Nature Communications

https://doi.org/10.1038/s41467-026-70801-9

Article in Press

RNA functional modulation by Mitoxantrone via RNA structural ensemble repartitioning

Received: 18 September 2025

Accepted: 3 March 2026

Cite this article as: Zhang, C., Borovská, I., Iobashvili, T. *et al.* RNA functional modulation by Mitoxantrone via RNA structural ensemble repartitioning. *Nat Commun* (2026). https://doi.org/10.1038/s41467-026-70801-9

Chundan Zhang, Ivana Borovská, Teona Iobashvili, Edoardo Morandi, Marta Lionnez, Oluwatosin S. Olayinka, Rinse de Boer, Massimiliano Clamer, Martin D. Witte, Klaus Pors, John S. Schneekloth Jr. & Danny Incarnato

RNA functional modulation by Mitoxantrone via RNA structural ensemble repartitioning

Chundan Zhang[1†], Ivana Borovská[1,2†], Teona Iobashvili[1], Edoardo Morandi[1], Marta Lionnez[3], Oluwatosin S. Olayinka[4], Rinse de Boer[5], Massimiliano Clamer[6], Martin D. Witte[3], Klaus Pors[4], John S. Schneekloth Jr.[7] and Danny Incarnato[1*]

[1] Department of Molecular Genetics, Groningen Biomolecular Sciences and Biotechnology Institute (GBB), University of Groningen, Groningen, the Netherlands

[2] Institute of Molecular Physiology and Genetics, Centre of Biosciences, Slovak Academy of Sciences, Bratislava 840 05, Slovak Republic

[3] Stratingh Institute for Chemistry, University of Groningen, the Netherlands

[4] Institute of Cancer Therapeutics, Faculty of Health and Social Care, University of Bradford, Bradford, West Yorkshire, BD7 1DP, UK

[5] Department of Molecular Immunology and Microbiology, Groningen Biomolecular Sciences and Biotechnology Institute, University of Groningen, Groningen, the Netherlands

[6] IMMAGINA Biotechnology S.r.l., Viale dell'Industria 47, 38057 Pergine Valsugana (TN) Italy

[7] Chemical Biology Laboratory, Center for Cancer Research, National Cancer Institute, Frederick, MD 21702-1201 USA

† Equal contribution

* Corresponding author, Email: d.incarnato@rug.nl

Abstract

Targeting RNA with small molecules offers a strategy to modulate gene expression at undruggable targets. Traditional screens favor thermodynamically stable, low-entropy RNA motifs with defined conformations, yet these provide limited energetic leverage for functional modulation. Many RNAs instead sample dynamic structural ensembles that small molecules can stabilize or redirect. Using group I self-splicing introns as a model, we identified the antineoplastic drug Mitoxantrone as a competitive inhibitor of RNA self-splicing (IC_{50} = 4.3 μM) that stabilizes the native conformation of the T4 td intron. Structure-activity analysis showed the anthraquinone scaffold alone is insufficient, and basic amine side chains are required for RNA structural modulation. Transcriptome-wide chemical probing in human cells revealed preferential binding to GC-rich structured regions, although only a subset showed structural change. Furthermore, global analysis of 5′ UTR ensembles showed reduced structural heterogeneity and increased translation, demonstrating functional repartitioning of RNA conformational landscapes.

Introduction

Targeting of RNA with small molecules has emerged, over the past decade, as a promising new modality for treating currently undruggable diseases[1,2].

RNA molecules are single-stranded and can fold back on themselves to create complex secondary and tertiary structures. Just like proteins, RNA structures can form ligandable pockets[3,4], which are amenable to targeting with small molecule drugs. Many RNA molecules can sample a vast conformational space, populating an ensemble of alternative structures, as opposed to proteins, which frequently have well-ordered tertiary structure[5–9]. While the ability to dynamically switch between these alternative structural states is paramount to many of the regulatory functions of RNA, the inherent structural flexibility of RNA molecules is typically seen as a disadvantage for the identification of small molecule binders. Often, low-entropy RNA structural elements[10–12], meaning regions of RNA molecules that adopt fewer, well-defined conformations, tend to be regarded as better targets and, therefore, to be favored over highly structurally-heterogeneous regions[1,13]. However, the energetic contributions of small molecules are often insufficient to induce significant conformational changes in stable RNA structures[14]. Conversely, small molecules can potently modulate the conformational energy landscape for an RNA[9], for example by selecting and stabilizing specific conformations in the ensemble (conformational selection), or by inducing the formation of a (possibly novel) alternative structure (induced fit). Such mechanisms have been previously reported in riboswitches[15–17], which are segments of (typically bacterial) mRNAs capable of dynamically changing their structure upon binding of a small molecule ligand, to regulate gene expression[18], as well as for recently reported inhibitors targeting the SARS-CoV-2 frameshifting element[19] (FSE), among others. Notably, the mechanism of action of Risdiplam[20], the sole FDA-approved mRNA-targeted drug, used for the treatment of Spinal Muscular Atrophy (SMA), involves the stabilization of the otherwise unstable bulged heteroduplex formed between the 5′ splice site of exon 7 in SMN2 pre-mRNA, as well as other 5′ splice sites[21], and the RNA component of the U1 snRNP[22,23].

A variety of methods have been adopted to identify small molecule RNA binders, including two-dimensional combinatorial screening[24,25], small molecule microarrays[26,27] (SMMs), fluorescence-based assays[28,29], fragment screening via NMR spectroscopy[30,31] or RNA chemical probing[32], and affinity selection mass spectrometry (AS-MS), such as automated ligand identification system[33–35] (ALIS). However, all of these methods are heavily biased towards the identification of binders, which often do not elicit any functional response[2]. Consequently, despite several attempts to define physicochemical properties of privileged RNA-binding chemical scaffolds[36,34,37–39], the identification of functional RNA binders still represents an open challenge.

While the aforementioned methods are typically limited to the analysis of individual RNA targets, approaches like Chem-CLIP, icCL-seq and PEARL-seq[40–45] can enable the transcriptome-wide identification of small molecule binding events within cells. These techniques are based on the functionalization of small molecules with photocrosslinkable moieties (e.g., diazirines), hence enabling their covalent attachment of the candidate small molecule to the interacting RNAs upon irradiation with long wavelength UV light. After crosslinking the small molecule is recovered together with its RNA partners, typically by exploiting an azide handle that enables its biotinylation and recovery via streptavidin beads. Alternatively, a recently proposed approach exploited the functionalization of drugs with an acylimidazole moiety, which enabled direct mapping of RNA-drug interactions via sequencing-based detection of adducts formed between the 2′-hydroxyl of ribose and the small molecule[46,47]. In general, these methods are limited to detecting RNA-small molecule binding events, without providing any direct insight into the functional outcomes of these interactions.

Conversely, chemical probing methods offer the unique advantage of simultaneously mapping small molecule binding sites[48] and the resulting functional consequences on RNA structure[32,44,49]. Additionally, chemical probing does not require modification of the small molecule with a tag that has the potential to alter its binding profile. By leveraging the differential reactivity of RNA nucleotides to chemical probes in the presence or absence of small molecules, these techniques can in principle reveal ligand-induced structural changes at nucleotide resolution across entire transcriptomes. This enables not only the identification of RNA regions directly bound by a small molecule but also the elucidation of downstream structural changes that may underlie functional effects. As such, chemical probing represents a powerful strategy to bridge the gap between binding and function, providing critical insight into the mechanism of action of RNA-targeted small molecules in a cellular context. Furthermore, recent computational advances[50–53] have paved the way for the deconvolution of RNA structural ensembles from transcriptome-wide chemical probing experiments, possibly enabling, for the first time, the systematic investigation of how small molecules can repartition RNA conformational landscapes on a transcriptome scale.

In this study, by using the T4 *td* self-splicing group I intron as a model RNA, we first screened a small molecule library biased towards compounds with RNA-binding features and identified Mitoxantrone[54], an FDA-approved antineoplastic anthraquinone drug, as a general inhibitor of group I intron self-splicing. Ensemble deconvolution analysis of the T4 *td* intron suggested that Mitoxantrone stabilizes the intron's structure via conformational selection. By leveraging transcriptome-wide chemical probing analysis of human cells treated with Mitoxantrone we obtained insights into the binding preferences of this drug, unexpectedly showing that only a

discrete subset of the sites bound by Mitoxantrone shows any detectable reactivity change, typically reflecting an increased RNA stability. Transcriptome-scale mapping of 5′ UTR structural ensembles further revealed extensive changes in ensemble partitioning upon treatment with Mitoxantrone, further confirming the ability of Mitoxantrone to repartition RNA conformational energy landscapes.

Results

Functional screening identifies Mitoxantrone as a general group I intron self-splicing inhibitor

To identify preferential chemical scaffolds that could modulate RNA structure and function, we devised a fast high-throughput sequencing-based screening platform, using the T4 *td* group I self-splicing intron[55,56] as model RNA (Fig. 1a). Group I introns adopt a complex and highly-conserved structure[57] that mediates their self-splicing in the presence of GTP (or other guanosine nucleotides) as cofactor. In this setup, a template DNA containing the intron flanked by two short exons is transcribed by the T7 RNA polymerase, in the presence of different compounds. Splicing efficiency is then monitored by targeted RT-PCR and sequencing of the spliced and unspliced RNA species. To maximize the chances of identifying compounds capable of modulating RNA function, which would also be suited for therapeutic use, we biased our library towards FDA-approved compounds showing close structural similarity to small molecules identified as RNA binders by a recent large-scale microarray-based screening[39] (Supplementary Data 1). Furthermore, we enriched our selection with FDA-approved kinase inhibitors, as compelling evidence exists that these compounds constitute preferential RNA binders[58–60], resulting in a library of 156 small molecules. As a positive control, we included neomycin, a known inhibitor of group I intron self-splicing[61–64], at two different concentrations (100 μM and 500 μM). DMSO-treated reactions showed efficient co-transcriptional splicing (median % spliced: 94.4%), while neomycin treatment consistently resulted into moderate to strong splicing inhibition (median % spliced at 100 μM: 89.3%, $P = 2.0 \times 10^{-3}$; median % spliced at 500 μM: 15.7%, $P = 2.9 \times 10^{-4}$; one-tailed Wilcoxon rank sum test), hence confirming the ability of our approach to capture small molecule-mediated splicing modulations (Fig. 1b). As expected, the vast majority of our library showed limited to no inhibition of splicing at 50 μM (median % spliced: 95.0%, $P = 0.95$; one-tailed Wilcoxon rank sum test), with a single compound, Mitoxantone[54] (MTX), an antineoplastic synthetic anthraquinone drug, showing near complete inhibition. To determine the potency of MTX as group I self-splicing inhibitor, we exploited the same screening platform to perform an MTX titration curve on the T4 *td* intron, which revealed an IC_{50} of 4.3 μM (Fig. 1c). To assess whether the inhibitory effect of MTX could also be generalized to other group I introns, we performed the same analysis on a group I intron located within the 25S rRNA gene of *C. albicans*[65], which revealed a similar IC_{50} (4.4 μM) (Supplementary Fig. 1a). To rule out that the observed MTX inhibition might be due to unexpected effects on T7 transcription, we further confirmed its ability to inhibit splicing of the T4 *td* intron in an *in vitro* splicing assay containing the sole refolded full-

length RNA and GTP (Supplementary Fig. 1b). We further investigated whether the inhibitory mechanism of MTX was non-competitive, as for certain aminoglycoside antibiotics[61,62], or competitive, as for deoxyguanosine, arginine, streptomycin and other recently discovered inhibitors[66–70]. Competition of an inhibitory concentration of MTX with increasing concentrations of GTP showed partial rescue of T4 *td* intron self-splicing, both co-transcriptionally (Fig. 1d) and in an *in vitro* splicing assay (Supplementary Fig. 1c), hence suggesting that MTX and GTP compete for binding to the ωG-binding pocket. However, given the intercalating nature of MTX and the incomplete rescue observed even with a 500-fold molar excess of GTP, MTX-mediated inhibition may in part reflect allosteric effects due to binding at additional sites.

Altogether, these results demonstrate that MTX is a potent and general competitive inhibitor of group I intron self-splicing.

QSAR analysis of anthraquinone compounds reveals physicochemical features linked to Mitoxantrone activity as a splicing inhibitor

To gain insights into the structure-activity relationships (SAR) driving MTX's ability to inhibit group I intron self-splicing, we evaluated a focused library of both natural and synthetic[71–76] anthraquinone compounds similar to MTX (Supplementary Fig. 2). Compounds were tested at a single dose (50 µM) on both T4 *td* and *C. albicans* 25S rRNA introns, using our co-transcriptional sequencing-based assay (Fig. 2a). The response of the two introns to the tested compounds was highly correlated (r = 0.97, Pearson correlation coefficient) (Fig. 2b), indicating a conserved mechanism of action for group I splicing inhibition by anthraquinone-based compounds. Thanks to their planar, aromatic core, anthraquinones are known to broadly intercalate into both DNA and RNA duplexes[77–82], possibly affecting base stacking and the integrity of nucleic acid helices. MTX's primary mechanism of action occurs through intercalation[83], whereby it inhibits type IIA topoisomerases[84], and inhibits DNA synthesis and repair, although it has also been shown to bind to RNA[79,85–87]. The six natural anthraquinones in our library (Anthraquinone, Aloe emodin, Emodin, Chrysophanol, Physcion and Quinizarin), all differing only slightly in substitution patterns on the anthraquinone pharmacophore, showed negligible splicing inhibition (average <2%). This suggests that, while intercalation may mediate general nucleic acid binding, it does not by itself drive functional inhibition in this context. Quantitative SAR (QSAR) analysis (Fig. 2c, Supplementary Fig. 3 and Supplementary Data 2) revealed strong positive correlations between the measured average percent inhibition and physicochemical features associated with hydrogen bonding, including number of NH and OH groups (r = 0.76, Pearson correlation coefficient), hydrogen bond donors (r = 0.72, Pearson correlation coefficient), particularly secondary amines

(r = 0.59, Pearson correlation coefficient), hydrogen bond acceptors (r = 0.60, Pearson correlation coefficient), and topological polar surface area (TPSA) (r = 0.64, Pearson correlation coefficient). These findings point toward hydrogen bonding capacity, rather than intercalation, as a key determinant of functional activity.

Consistently, the most active synthetic anthraquinones in our library, including Pixantrone[88], KP300, KP311, KP312, KP315, KP105, and KP110[73,74], all featured side chains containing basic amines that are likely protonated at physiological pH. These groups are well suited to mediate electrostatic and hydrogen bond interactions with RNA nucleobases and the phosphodiester backbone, in line with a previous NMR study[79] showing MTX interacting with a stem-loop in the *MAPT* pre-mRNA via its side chains (Supplementary Fig. 4). In contrast, compounds bearing neutral or quaternary ammonium side chains, such as Banoxantrone[89], were largely inactive, reinforcing the importance of both hydrogen bonding and appropriate charge presentation.

To directly test the contribution of basic amine side chains, we synthesized four derivatives of Quinizarin, a natural anthraquinone showing no detectable activity in our assay (< 1% inhibition), with varying substitutions (Supplementary Fig. 5). Of these, only compound 3 (average inhibition: ~7.7% for T4 *td* intron, ~13.8% for *C. albicans* 25S rRNA intron) and compound 4 (average inhibition: ~30.5% for T4 *td* intron, ~64.8% for *C. albicans* 25S rRNA intron) showed functional activity (Fig. 2d). Unlike compound 3, which harbors a secondary amine in the side chain, and shares some similarities with KP312 and KP315, compound 4 features an amide in its backbone. The higher potency of compound 4 compared to compound 3 may stem from the ability of amides to form hydrogen bond interactions with nucleobases and the presence of an additional primary amine, similar to side chains found in Pixantrone. In contrast, compound 2, despite carrying a quaternary ammonium and a triazole moiety, failed to inhibit splicing, mirroring our observations with Banoxantrone.

Interestingly, several of the more potent compounds, including Pixantrone and compound 4, possess multiple basic amines on flexible side chains, raising the possibility that multivalent interactions may enhance affinity or specificity for structured RNA elements. Moreover, the geometry and spatial orientation of hydrogen bond donors may also be critical, as proper alignment with RNA grooves, bulges, or backbone phosphodiesters might be required for productive binding in the absence of protein cofactors.

Comparative analysis between active and inactive compounds further highlighted features that appear dispensable for productive binding: (1) hydroxyl groups at positions 5 and 8 of the anthraquinone core, absent in Pixantrone and active derivatives; (2) secondary amines at positions 1 and 4, which are also missing in compounds 3 and 4; and (3) terminal hydroxyls on

MTX's side chains, which are absent in compound 4, despite its greater potency compared to compound 3. Nonetheless, most active compounds retained at least one terminal hydrogen bond donor on their side chains, suggesting that this feature likely contributes positively to RNA engagement and inhibition.

Taken together, our data indicate that, while the intercalative core of MTX facilitates RNA binding, it is the presence of amine-functionalized, hydrogen-bonding side chains, with suitable geometry, flexibility, and protonation state, that differentiates binding mode and is essential for functional modulation of RNA splicing.

Mitoxantrone stabilizes the native T4 *td* group I intron conformation

We next sought to investigate the structural consequences of MTX binding to the T4 *td* intron, by interrogating its structure by chemical probing with dimethyl sulfate (DMS) coupled with mutational profiling analysis (DMS-MaPseq[90]) upon *in vitro* refolding, in the presence or absence of an inhibitory concentration of MTX. Although MTX has been shown to bind and stabilize non-canonical DNA secondary structures[75,91], a study conducted on group II self-splicing introns suggested that MTX can act as a non-competitive inhibitor by disrupting stable RNA folds[92], as previously observed[85]. Therefore, for comparison, we also performed DMS-MaPseq analysis on the intron probed under denaturing conditions. Receiver Operator Characteristic (ROC) curve analysis of bulk DMS signal (Fig. 3a) showed strong agreement between DMS reactivities for both control (AUC = 0.84) and MTX treatment (AUC = 0.86) and the known intron's structure[57], which was instead lost upon denaturation (AUC = 0.34). ΔDMS analysis of the MTX-treated intron versus control showed a generalized decrease in reactivity towards DMS, particularly in base-paired regions, in the presence of MTX (Supplementary Fig. 6). Furthermore, comparison of the distribution of DMS reactivities for paired versus unpaired bases in the T4 *td* intron reference structure showed a sharper separation upon MTX treatment ($P = 7.2 \times 10^{-10}$, one-tailed Wilcoxon rank sum test) as compared to control ($P = 4.6 \times 10^{-9}$, one-tailed Wilcoxon rank sum test), with unpaired bases having median reactivity 3.2-fold higher than paired bases for the MTX-treated intron (paired: 0.23; unpaired: 0.74), as compared to just 1.9-fold for the control (paired: 0.36; unpaired: 0.69) (Fig. 3b). Such a difference was also reflected by a higher Gini index for the MTX-treated intron (0.39) as compared to the control (0.29), hence suggesting that MTX binding to the T4 *td* intron does not broadly disrupt its folding, but rather has a net stabilizing effect.

We wondered whether the observed stabilization was a consequence of a reduced conformational heterogeneity in the T4 *td* intron's ensemble. Ensemble deconvolution analysis of DMS-MaPseq data using the DRACO algorithm[51] (Fig. 3c) revealed the existence of two distinct structural states

(A: 63.2 ± 0.95% and B: 36.8 ± 0.95%) within the control ensemble, one of which (B) readily disappeared upon MTX treatment. Secondary structure modelling using optimized folding parameters (Supplementary Fig. 7) showed that state A adopts a very stable fold (median Shannon entropy: 0.002 for both control and MTX-treated intron), corresponding to the known T4 *td* structure (mFMI: 0.9) (Supplementary Fig. 8a), while state B exhibits one order of magnitude higher disorder (median Shannon entropy: 0.02), particularly affecting helix P3 and part of the catalytic core, and likely represents an aggregate of multiple misfolded conformations. Prior studies conducted on group I introns showed that these RNAs present rugged conformational landscapes *in vitro*, populated by several long-lived misfolded intermediates[93–101]. Accordingly, under our experimental conditions, we could consistently observe that ~33.6 ± 2% of the RNA remained unspliced for up to one-hour post-refolding, which is in line with DRACO's abundance estimate for state B (Supplementary Fig. 8b). Notably, addition of excess GTP to the MTX-treated intron (Supplementary Fig. 8c) led to reappearance of state B (Supplementary Fig. 8d), in agreement with the above proposed mechanism of action of MTX as competitive inhibitor. Altogether, these results demonstrate that MTX binding results in a stabilization of the native T4 *td* intron's conformation within the ensemble, further suggesting a conformational selection mechanism.

Transcriptome-wide RNA structure analysis of cells treated with Mitoxantrone provides insights into its binding preferences and structural effects

Intrigued by these results, we decided to investigate the extent to which MTX might represent a preferential scaffold for RNA structural modulation, by performing transcriptome-wide RNA structure interrogation in living cells. Triple-negative breast cancer MDA-MB-231 cells were treated, in biological duplicate, with 10 μM MTX, or DMSO, and subjected to selective 2′-hydroxyl acylation analyzed by primer extension (SHAPE) analysis with the 2A3 probe[102], followed by mutational profiling and sequencing (SHAPE-MaP[10,103]). Previous studies showed that MTX uptake begins within seconds and it reaches steady-state in around 30 minutes[104]. To minimize any indirect or secondary effects stemming from other activities of MTX, we decided to treat cells with MTX for just 30 minutes and confirmed cell uptake of MTX via fluorescence microscopy[105] (Supplementary Fig. 9). As, to the best of our knowledge, 2A3 has never been used before for transcriptome-wide SHAPE-MaP analyses, we first confirmed that our data met minimum quality standards. As compared to an untreated DMSO-treated control, 2A3 probing only marginally increased the rate of multi-mapping reads, while retaining ~80% uniquely aligned reads (Supplementary Fig. 10a). On average, ~71.7% of the alignments from 2A3-probed samples

harbored mutations, as compared to just ~27.2% for control samples (Supplementary Fig. 10b), which included a large fraction of deletions and insertions, in line with the known mutational signature of the SuperScript II reverse transcriptase in SHAPE-MaP experiments[10] (Supplementary Fig. 10c), without exhibiting any particular nucleobase preference (Supplementary Fig. 10d). Overall, we obtained structural information across ~4,500 transcripts. Comparison of RNA structuromes in sliding windows revealed high reproducibility of SHAPE signals across replicates for both DMSO (r = 0.84, Pearson correlation coefficient) and MTX-treated (r = 0.87, Pearson correlation coefficient) cells (Supplementary Fig. 11). Somewhat unexpectedly, given MTX binding through intercalation, SHAPE profiles remained highly similar even when comparing MTX to DMSO treatment (median r = 0.80, Pearson correlation coefficient) (Fig. 4a), suggesting that MTX does not induce widespread – but rather, localized – changes in RNA structure. Similarly, the change in Gini index was minimal (median: -0.005), indicating no evidence of widespread RNA refolding or unfolding. Accordingly, structure modelling of the transcriptomes of DMSO and MTX-treated cells using optimized folding parameters (Supplementary Fig. 12) showed extremely high structural similarity, as measured by modified Fowlkes-Mallows index[106] (mFMI) (median: 1), with ~72% of the windows having mFMI of at least 0.8 (Fig. 4b). To identify putative MTX binding sites across the transcriptome, we first sought to identify bases showing strong protection or deprotection from SHAPE treatment in MTX treated cells. Under stringent selection criteria (see Methods) we identified 166,227 bases (Supplementary Data 3), of which approximately 54.5% and 45.5% respectively showed protection or deprotection upon MTX treatment (Supplementary Fig. 13a). Base enrichment analysis showed that these bases were significantly enriched for Cs and Gs and depleted of As and Us (Supplementary Fig. 13b). Stratification of bases by differential SHAPE reactivity upon MTX treatment further revealed that Gs were preferentially enriched among protected bases (P = 9.2 x 10^{-141}, two-tailed binomial test), while deprotected bases were preferentially enriched for Cs (P = 2.5 x 10^{-269}, two-tailed binomial test) (Fig. 4c). As anthraquinone derivatives have been previously shown to be able to bind to RNA G-quadruplex (rG4) structures[107], we wondered whether this enhanced protection of Gs upon MTX treatment might be the result of a widespread stabilization of rG4s in the transcriptome. Although differentially (de)protected bases showed a moderate enrichment for rG4-forming regions[108] (P = 2.7 x 10^{-5}, one-sided binomial test), this only accounted for 966 bases within 405 rG4s, corresponding to less than 0.6% of the identified sites, hence suggesting that rG4s do not generally constitute MTX's preferred target. Instead, we observed a significant enrichment of differentially (de)protected bases within base-paired regions relative to a random set of unchanged bases of matching size (P < 10^{-323}, one-tailed binomial

test), in agreement with MTX binding to RNA via intercalation. To gain insights into MTX binding preferences, we next analyzed the frequency of neighboring base-pairs at sites of differential protection by MTX. We consistently observed a massive enrichment for neighboring GC-rich base-pairs (CG/CG, GC/GC and CG/GC, $P = 9.9 \times 10^{-324}$, followed by GC/CG, $P = 3.9 \times 10^{-43}$, two-tailed binomial test), and an equally robust depletion for neighboring AU-rich base-pairs ($P = 4.9 \times 10^{-324}$, two-tailed binomial test) (Fig. 4d), irrespective of whether SHAPE data from DMSO or MTX-treated cells was used for structure modelling (Supplementary Fig. 13c). Notably, in light of these findings, we revisited DMS reactivity data for the T4 *td* intron and found that the helices exhibiting the highest median MTX-induced DMS reactivity fold change were P4 (scaffolding domain) and P7.1 (catalytic domain), which contain the highest number of stacked GC-rich base-pairs in the entire structure (4 and 3, respectively).

These results agree with previous reports on the DNA binding preference for CpG sites of MTX[109–112] and nogalamycin[113], an anthracycline antibiotic, as well as with the published NMR-derived structure of MTX in complex with a stem-loop in the *MAPT* pre-mRNA, in which MTX is stacked between two neighboring GC-containing base-pairs (Supplementary Fig. 4). Furthermore, as previously discussed for the QSAR analysis, the 3D structure of the *MAPT* stem-loop shows that the amines in one of MTX's side chains can compete with the N4 of cytosine for hydrogen bonding to the O6 of guanine. Such binding modality provides a plausible rationale for the increased protection of Gs and deprotection of Cs from 2A3 probing upon MTX treatment. It is conceivable that hydrogen bonding of the amines in MTX's side chains to guanine might result in reduced structural flexibility of Gs, consequently increasing the flexibility of interacting Cs. Accordingly, we found that the fraction of differentially protected bases predicted to interact with deprotected bases (with a base-pairing tolerance of ±2 nucleotides) was significantly higher than expected by chance for a random equally-large set of unchanged bases ($P = 8.0 \times 10^{-64}$, one-tailed binomial test). While this only accounted for ~8% of the differentially protected bases, this likely reflects several methodological and biological factors. First, putative MTX binding sites were defined using a stringent reactivity fold change threshold, such that the base-pairing partner of a differentially protected nucleotide may not itself have passed this cutoff. Second, SHAPE-MaP reports an ensemble-averaged signal, and the secondary structures used for this analysis represent only one (or the average of a subset) of the conformations populated in cell, potentially obscuring base-pairing relationships present in alternative states. Finally, some differential protections may arise indirectly from local structural rearrangements, in which destabilization of one element promotes the formation of a more stable alternative structure rather than preserving the original pairing interaction. Furthermore, bases showing differential protection upon MTX treatment were

not randomly distributed within the transcriptome, but rather they tended to cluster in strict proximity, with a median distance of 4 nucleotides to the closest differentially protected base, and approximately 97.6% of the bases falling within 50 nucleotides from each other (Fig. 4e).

To further investigate the structural consequences of MTX binding, we analyzed the structuredness of regions immediately surrounding differentially protected sites. We observed that MTX binding was accompanied by a significant increase in Gini index (median DMSO: 0.33; median MTX: 0.37; $P < 10^{-323}$, paired Wilcoxon rank sum test) and a moderate yet significant decrease in median SHAPE reactivity (median DMSO: 0.26; median MTX: 0.25; $P = 2.6 \times 10^{-150}$, paired Wilcoxon rank sum test) (Fig. 4f), in agreement with the stabilizing effect of MTX observed for the T4 *td* intron. We next devised a simple strategy to identify regions with consistent SHAPE reactivity profiles across both DMSO and MTX-treated cells, as well as regions showing robust SHAPE reactivity changes upon MTX binding (see Methods). Using stringent selection criteria, we identified a total of 40,345 regions, encompassing ~1.6 million bases, of which ~13.3% exhibiting MTX-induced reactivity changes (Fig. 4g, Supplementary Fig. 13d and Supplementary Data 4). We further confirmed the dose-dependent relationship between MTX concentration and SHAPE reactivity for a subset of these sites via targeted SHAPE-MaP analysis (Supplementary Fig. 14). The observed saturable behavior indicates that the measured reactivity changes are the result of specific MTX binding events. We wondered whether the observed alterations in SHAPE reactivity were a consequence of the MTX-dependent disruption of protein binding, however we did not observe any enrichment for protein-bound regions from ENCORE eCLIP data[114]. Rather, these regions appeared to be significantly depleted for RNA-binding protein (RBP) binding sites as compared to a random set of unchanged regions of matching size ($P = 7.7 \times 10^{-13}$, one-sided binomial test), which is in line with MTX's preference for binding to structured regions, as opposed to the generalized preference of RBPs for binding to single-stranded, unstructured contexts[115–119].

Notably, while over 63% of the transcriptome regions passing our stringent selection overlapped with sites of differential protection by MTX, only ~30.7% of them, encompassing ~350,000 bases (~21.6%), showed any detectable SHAPE reactivity change. Although differential protection might occur for reasons other than direct MTX binding, our results suggest that only a small subset of MTX binding events might actually elicit structural, and possibly functional, changes.

Mitoxantrone redistributes 5′ UTR RNA structural ensembles in living cells

To further explore the impact of MTX binding on RNA conformational ensembles in living cells, we proceeded to perform ensemble deconvolution analysis. As this type of analysis is extremely demanding in terms of required sequencing depth, we leveraged the 5′UTR-MaP methodology we recently introduced[120], which enables the selective enrichment of 5′ UTRs (Supplementary Fig. 15a) and, more generally, of 5′-terminal regions of capped transcripts. This time we opted for DMS probing over SHAPE as the reverse transcriptases typically used for DMS-MaPseq analyses can non-ambiguously record over 95% of the DMS-modified sites as point mutations[90], hence achieving superior signal-to-noise ratio, and making DMS a better probe for ensemble deconvolution analyses. As expected, we observed an enrichment for DMS-induced modifications on A and C bases, which accounted for ~90% of the mutations (Supplementary Fig. 15b). DMS reactivities showed excellent correlation between biological replicates (r = 0.94-0.95, Pearson correlation coefficient) and, in line with our observations from transcriptome-wide SHAPE-MaP analysis, MTX treatment only had a limited effect on the structure of the 5′ UTRome as compared to DMSO (r = 0.92, Pearson correlation coefficient) (Supplementary Fig. 15c).

We achieved sufficient depth for ensemble deconvolution analysis across ~140,000 bases, spanning nearly 1,000 transcripts. DRACO-mediated ensemble deconvolution showed that ~45% of the analyzed bases populated two or more conformations across 553 transcripts in DMSO-treated cells, as compared to ~40.5% across 526 transcripts for MTX-treated cells (Fig. 5a and Supplementary Data 5). Of the ~130,000 bases common to both conditions, ~20.2% showed reduced ensemble heterogeneity upon MTX treatment, as compared to ~16.5% for which heterogeneity increased (Fig. 5b). Interestingly, although ensemble composition did not appear to change for approximately 63.3% of the analyzed bases, the relative abundances of the deconvolved conformations changed substantially between DMSO and MTX-treated cells (r = 0.60-0.62, Pearson correlation coefficient), while it stays consistent between biological replicates of the same condition (r = 0.98 for DMSO, r = 0.93 for MTX, Pearson correlation coefficient) (Fig. 5c). These results are in line with our prior observations on the T4 *td* intron and provide further evidence for the ability of MTX to modulate the partitioning of RNA structural ensembles (Fig. 5d and Supplementary Fig. 16a).

As 5′ UTR structural ensemble dynamics play a key role in translational regulation, we further sought to evaluate the functional consequences of MTX-induced repartitioning of 5′ UTR conformational ensembles by performing ribosome profiling via RiboLace[121], which exploits a biotin-labeled puromycin analog to enrich actively translating ribosomes. Notably, we observed a moderate yet significant increase in translation efficiencies 30 minutes post-MTX treatment for those mRNAs whose 5′ UTRs showed reduced ensemble heterogeneity (P = 8.6 x 10^{-3}, two-tailed

Wilcoxon rank sum test), while no statistically significant difference was observed for mRNAs whose 5′ UTRs showed an increase in ensemble heterogeneity, as compared to mRNAs whose 5′ UTRs showed no change in ensemble heterogeneity (Fig. 5e). Thus, showing that MTX-mediated conformational selection of 5′ UTR structural ensembles directly results in the modulation of mRNA translation efficiency.

Finally, we performed structure modelling of regions whose heterogeneity decreased upon MTX treatment, as well as of regions whose heterogeneity and relative conformation abundances remained similar between DMSO and MTX-treated cells (see Methods). We then analyzed the frequency of neighboring base-pairs in the conformations selected by MTX, as compared to those in the ensembles of DMSO-treated cells, as well as those in the ensembles that remained “stable” upon MTX treatment. We detected a significant enrichment for neighboring GC-rich base-pairs, particularly CG/CG (P = 1.7 x 10^{-18}, two-tailed binomial test), followed by GC/GC (P = 2.6 x 10^{-10}, two-tailed binomial test) and CG/GC (P = 3.2 x 10^{-5}, two-tailed binomial test) (Supplementary Fig. 16b), in line with our observations from transcriptome-wide SHAPE-MaP analysis, further strengthening the notion that MTX binding to these sites enables the stabilization of selected conformations within the ensemble.

Discussion

While numerous studies have focused on identifying small molecules that bind to RNA, the extent to which these interactions result in functional RNA modulation remains largely unexplored. In this study, we show that binding does not necessarily imply function, and that intercalation alone, although sufficient for general engagement with nucleic acids, is insufficient to confer activity. Instead, our results indicate that a specific geometry of interactions, particularly hydrogen bonds, is required to modulate RNA folding and have functional consequences.

Through a combination of functional screening, transcriptome-wide RNA chemical probing, and ensemble deconvolution, we identified Mitoxantrone (MTX) as a potent modulator of RNA structure and function. Although MTX is a well-characterized DNA intercalator, our data show that intercalation is not the principal driver of its activity on RNA, at least with respect to impacting translational effects. Natural anthraquinones that share the same planar aromatic core as MTX, but lack amine-containing side chains, are broadly inactive in splicing inhibition assays, despite presumably retaining similar intercalative potential. This suggests that the anthraquinone scaffold may primarily serve to anchor and position functionalized side chains that mediate more specific and productive interactions with RNA. Our QSAR analysis further supports this model, highlighting secondary amines and overall hydrogen bonding potential as key correlates of activity, in

agreement with previous studies showing polyamine-mediated stabilization of RNA structures[122–127]. Furthermore, our results on Quinizarin analogs indicate that the addition of similar side chains to inactive RNA binders might enable their conversion into functional RNA modulators.

Importantly, although transcriptome-wide RNA structure analysis suggests that MTX binds a large number of sites across the human transcriptome, only a fraction of these interactions result in detectable structural changes. This reinforces the notion that RNA binding alone is not a reliable predictor of function, and that productive engagement likely depends on both the molecular features of the compound and the local RNA context. Analysis of regions of differential MTX-induced protection from chemical probing revealed MTX preference for binding to GC-rich, structured elements, which are generally depleted of RNA-binding protein footprints and that the structural stability of these regions increases upon MTX binding. Ensemble deconvolution analysis of the T4 td intron and of human 5′ UTRs further corroborate this idea, revealing that MTX consistently stabilizes specific conformations within structural ensembles, supporting a conformational selection model.

By probing the structural landscape of 5′ UTRs on a transcriptome-scale, we further uncovered a clear connection between ensemble redistribution and translational output. Transcripts that exhibited reduced conformational heterogeneity upon MTX treatment showed significantly increased translation efficiency, suggesting that modulation of structural ensembles can have immediate regulatory consequences. Notably, this is in line with previous studies showing that polyamines can modulate 5′ UTR secondary structure to stimulate mRNA translation[125]. While the precise mechanisms remain to be elucidated, and likely differ on a per-RNA basis, we can speculate that the stabilization of selected conformations by MTX might hamper translation of upstream ORFs, which we recently showed to be enriched within structurally-heterogeneous regions of human 5′ UTRs or, more generally, alleviate other inhibitory RNA structural features such as RNA G-quadruplexes.

From a therapeutic standpoint, our findings underscore the power of targeting RNA conformational ensembles rather than single well-defined structures. Small molecules that can redistribute structural ensembles within pathologically-relevant RNAs, for example by stabilizing specific conformers or by shifting structural equilibria, represent a promising avenue for modulating RNA function with high specificity. By extending the notion of druggability from fixed structural motifs to dynamic ensembles, ensemble-based targeting has the potential to unlock previously inaccessible RNA targets, including non-coding RNAs, structured 5′ and 3′ UTRs, and regulatory intronic elements.

In the context of the current state-of-the-art, our work fills an important gap. Existing transcriptome-wide techniques for mapping RNA-small molecule interactions are heavily biased toward identifying binding sites and typically provide little to no information on functional consequences. To our knowledge, this study represents the first systematic investigation of the transcriptome-wide structural and functional impact of a small molecule on RNA ensembles in living cells. Additionally, interrogating RNA-binding events and alteration of conformational ensembles via structure probing facilitates the study of RNA-targeted small molecules transcriptome-wide without the necessity of labeling the small molecule with a reactive sidechain. Indeed, it has previously been shown that minimal changes to small molecules can have a dramatic effect on binding to RNA targets[43,128]. By combining chemical probing, ensemble deconvolution, and translation profiling, we introduce a generalizable framework capable of distinguishing between inert and functionally productive binding events with (near) nucleotide resolution in cells.

Looking forward, this framework could be directly extended to systematically define ideal druggable sites within mRNAs and to guide the discovery of new RNA-targeted small molecules. Transcriptome-wide structure probing combined with ensemble deconvolution enables the identification of RNA regions that are both structurally dynamic and selectively responsive to small-molecule binding, features that are likely to confer heightened sensitivity to chemical modulation. Such regions could be prioritized as candidate druggable sites based on measurable criteria, including intrinsic structural plasticity, GC%, structuredness, and the magnitude of ligand-induced ensemble repartitioning. Coupling this strategy with focused chemical libraries or fragment-based screening, followed by iterative structure-guided optimization, would enable the rational discovery of small molecules tailored to selectively stabilize or destabilize specific RNA conformers within disease-relevant mRNAs.

While our approach offers important new insights, several limitations should be acknowledged. First, ensemble deconvolution methods remain limited in their ability to detect low-abundance or short-lived conformations, which may result in an underestimation of structural diversity and small molecule effects. Second, although we minimized indirect effects by using short MTX treatments, the possibility of secondary/indirect consequences cannot be completely ruled out. Future studies using orthogonal probing chemistries, improved conformational modeling algorithms, and time-resolved analyses will likely address some of these limitations.

Nevertheless, the conceptual framework and experimental toolkit presented here provide a powerful foundation for dissecting the functional landscape of RNA-small molecule interactions. By focusing on structural consequences rather than binding affinity alone, and by treating RNA

as a dynamic ensemble of conformations rather than a static scaffold, we outline a new direction for RNA-targeted therapeutic development: one that emphasizes functionally-informed design and the targeting of structural plasticity at scale.

Methods

Compound selection and screening.

Compounds from a library of FDA-approved compounds (cat. L1021, APExBIO) were selected by similarity to RNA binders identified in a recent large-scale screening[39]. Selection was performed using DataWarrior[129] and a similarity threshold of 90%. The final selection was further enriched with a set of 76 kinase inhibitors from the same library, yielding a total of 156 compounds (Supplementary Data 1). Screening plates included 7 negative control wells containing 2.5% DMSO, and 14 positive control wells containing Neomycin (cat. N1876, Merck) (7 of which at a concentration of 500 µM and 7 at a concentration of 2.5 M). Screening was performed in 5 µl reactions. First, reactions were assembled by mixing 50 ng of a dsDNA template harboring the T7 promoter followed by 50 nt exon 1 + group I intron + 50 nt exon 2, 0.2 µl T7 RNA Polymerase Mix (part of the HiScribe® T7 High Yield RNA Synthesis Kit; cat. E2040S, New England Biolabs), 0.1 µl SUPERase•In™ RNase Inhibitor (cat. A2696, ThermoFisher Scientific), 0.5 µl 10X T7 Reaction Buffer, and 1 µl of a 250 µM dilution in nuclease-free water of the compound to be tested. Reactions were incubated at 37°C for 2 min, after which 1 µl NTPs (2.5 mM each) was added to initiate the transcription reaction. Reactions were allowed to proceed for 5 min at 37°C, before terminating them by adding 1 µl 60.5 mM EDTA. Template DNA was degraded by adding 0.25 µl TURBO DNase I (cat. AM2239, ThermoFisher Scientific) and 1 µl 62.5 mM $CaCl_2$, and incubating at 37°C for 30 min. Transcribed RNA was purified using 1.8 volumes NucleoMag NGS Clean-up and Size Select beads (cat. 744970, Macherey Nagel) and eluted in 2.7 µl nuclease-free water. The eluted RNA was then mixed with 0.25 µl 10 µM RT1 (or RT2) reverse transcription primer (Supplementary Data 6), 0.25 µl dNTPs (10 mM each) and 0.5 µl 10X RT Buffer [500 mM Tris-HCl pH 8.0; 750 mM KCl]. Reactions were denatured by incubation at 70°C for 3 min, then snap-cooled on ice for 1 min. Reactions were then supplemented with 0.5 µl 100 mM DTT, 2 U SUPERase•In™ RNase Inhibitor, 40 U SuperScript™ II Reverse Transcriptase (cat. 18064022, ThermoFisher Scientific) and 0.5 µl 60 mM $MnCl_2$. Reverse transcription was carried out at 42°C for 30 min, followed by incubation at 75°C for 15 min to inactivate the reverse transcriptase. Reaction volumes were then brought to 10 µl with nuclease-free water and cDNA was purified using 0.9 volumes NucleoMag NGS Clean-up and Size Select beads. cDNA was eluted in 5 µl nuclease-free water and mixed with 2.5 µl 1 µM F1 (or F2) primer (Supplementary Data 6), 2.5 µl 10 µM i5 primer, 2.5 µl 10 µM i7 primer and 12.5 µl NEBNext® Ultra™ II Q5® Master Mix (cat. M0544X, New England Biolabs). PCR enrichment was performed as per manufacturer instructions. Amplified libraries were purified using 1 volume NucleoMag NGS Clean-up and Size Select beads.

The same experimental conditions were also used for the generation of dose-response curves (related to Fig. 1c and Supplementary Fig. 1a), for the GTP/$MgCl_2$ competition assay (related to Fig. 1d) and for the QSAR analysis (related to Fig. 2a). % splicing inhibition (related to Fig. 2a, b) was calculated as *min(0, 100 - % splicing relative to control)*.

Anthraquinone compounds.

Emodin (cat. E7881, Merck), Aloe-emodin (cat. 93938, Merck), Physcion (cat. 93893, Merck), Chrysophanol (cat. 229075, Merck), Quinizarin (cat. D0243, TCI Chemicals), Mitoxantrone (cat. M6545, Merck), Pixantrone (cat. SML2577, Merck), Banoxantrone (cat.

SML1854, Merck), Myra A (cat. M9823, Merck) were commercially available. KP39, KP105, KP110, KP145, KP312, KP353, KP365, ZP275 and SOM2 were synthesized as previously described[71–74,76]. Synthesis details for the remaining compounds are provided in Supplementary Note 1.

Synthesis of 2-aminopyridine-3-carboxylic acid imidazolide (2A3).

2-aminopyridine-3-carboxylic acid imidazolide (2A3) was synthesized as previously described, with minor changes. Briefly, 552.48 mg 2-aminopyridine-3-carboxylic acid (cat. A68300, Merck) and 648.6 mg 1,1′-Carbonyldiimidazole (CDI) (cat. 21860, Merck) were directly mixed in a 5 mL beaker with 4 mL DMSO anhydrous (cat. 276855, Merck) were added, and vigorously stirred at room temperature for 1 h. Residual unreacted powder was then removed by brief centrifugation at 17,000g for 2 min, after which the solution, assumed to represent a 1 M stock, was aliquoted in 50 µl aliquots and stored at -80°C.

Cell culture and *in vivo* probing.

Human MDA-MB-231 cells were cultured in high glucose DMEM medium (cat. L0104, Biowest), supplemented with 10% fetal bovine serum (FBS) (cat. H1138, Merck), 25 U/mL penicillin and 25 µg/mL streptomycin, at 37°C and 5% CO_2. Culture plates were pre-coated with 0.001% poly-L-lysine (cat. P8920, Merck) to ensure that cells would remain attached during probing. For drug treatment, cells were first washed once with PBS, prewarmed at 37°C. Then, Mitoxantrone (MTX) from a 10 mM stock in DMSO was mixed with fresh complete medium, prewarmed at 37°C, to achieve the desired final concentration (10 µM for transcriptome-wide analyses, or 0.1-0.5-1-5-10-25 µM for dose-response analysis), and the medium added to the cells. For control experiments, medium was mixed with an equivalent amount of neat DMSO. Cells were then incubated for 30 min at 37°C. For SHAPE probing, cells were washed twice with PBS, prewarmed at 37°C, to remove any traces of serum. 2A3 (or an equivalent volume of neat DMSO, for control experiments) was then mixed with fresh PBS, prewarmed at 37°C, and added to the cells. Cells were incubated at 37°C for 7.5 min. Reactions were then quenched by addition of 1 volume ice-cold 1 M DTT in PBS, after which the supernatant was aspired, cells were washed once in PBS, and then lysed by direct addition of 2 mL ice-cold TRIzol™ Reagent (cat. 15596018, ThermoFisher Scientific). For dimethyl sulfate (DMS) (cat. D186309, Merck) probing, DMS from a fresh 1:4 dilution in ethanol (~2.64 M) was directly added to the cells at a final concentration of 150 mM. Probing was conducted for 2 min at 37°C. Reactions were then quenched by addition of 1 volume 1 M DTT, after which cells were collected by centrifugation at 5,000g for 1 min. Supernatant was discarded and pellets were immediately lysed by direct addition of 1 mL ice-cold TRIzol™ Reagent.

Fluorescence microscopy analysis of MTX-treated cells.

Human MDA-MB-231 cells were plated on µ-Slide 8 Well coverslips (cat. 80827, Ibidi), pre-coated with 0.001% poly-L-lysine, at a density of 10^5 cells/well. 30 min prior to imaging, medium was replaced with 300 µl fresh medium containing either 10 µM final MTX, or an equivalent amount of neat DMSO. Coverslips were incubated at 37°C for 30 min before imaging on a Zeiss Observer Z1 (excitation: 587/25 nm; emission: 647/70 nm).

RNA extraction.

RNA samples in TRIzol™ were mixed with 0.2 volumes chloroform (cat. 319988, Merck) by vigorous vortexing for 15 sec, after which samples were allowed to sit at room temperature for 2 min, before centrifugation at 12,500g for 15 min (4°C). After phase separation, the upper aqueous phase was transferred to a clean 2 mL tube and mixed with 1 volume 2-propanol (cat. 190764, Merck) by vigorous vortexing for 15 sec. Samples were allowed to sit at room temperature for 10 min, before centrifugation at 17,000g for 10 min (4°C). Supernatant was discarded and the RNA pellet was washed twice in 75% ethanol. The RNA pellet was then allowed to air-dry for 10 min, before resuspension in nuclease-free water, pre-warmed at 70°C. Residual gDNA was removed by digestion I at 37°C for 30 min.

In vitro self-splicing assay.

As group I introns efficiently splice co-transcriptionally, *in vitro* transcription reactions typically yield very low amounts of full-length unspliced precursor. However, we found that addition of Urea at a final concentration of 1 M during transcription can efficiently inhibit co-transcriptional splicing, while preserving high transcription efficiency. Synthesis of the unspliced T4 *td* group I intron was performed in a reaction volume of 20 µl, using 200 ng dsDNA template, 2 µl 100 mM each NTP, 2 µl 10X T7 Reaction Buffer, 1 µl T7 RNA Polymerase Mix and 2.5 µl 8 M Urea, and by incubating at 37°C for 3 h. Template DNA was removed by digestion with TURBO DNase at 37°C for 30 min and RNA was purified on Monarch® Spin RNA Cleanup columns (10 µg) (cat. T2030L, New England Biolabs) as per manufacturer instructions. RNA was mixed with 1 volume 2X RNA Gel Loading Dye (cat. R0641, ThermoFisher Scientific), denatured at 70°C for 5 min, snap-cooled on ice and resolved on a 5% TBE-Urea polyacrylamide gel. The product corresponding to the full-length unspliced RNA (50 nt exon 1 + 265 nt intron + 50 nt exon 2) was excised and recovered by passive diffusion at 4°C for 16 h in 300 µl 0.05% SDS, supplemented with 60 U SUPERase•In™ RNase Inhibitor.

For *in vitro* refolding of the T4 *td* intron, 20 ng RNA in a volume of 2.5 µl were denatured at 55°C for 5 min and snap-cooled on ice for 1 min. 0.5 µl ice-cold 10X RNA Folding Buffer [400 mM Tris-HCl pH 7.5; 100 mM $MgCl_2$; 4 mM Spermidine] and 1 µl 500 µM GTP were then added, and RNA was incubated at 32°C for the 1 h. For experiments involving MTX, this was added at the desired concentration together with folding buffer and GTP.

DMS probing of *in vitro* refolded T4 *td* intron.

For *in vitro* probing of the refolded T4 *td* intron, 50 ng of full-length unspliced precursor in 41.5 µl nuclease-free water were denatured at 55°C for 5 min and snap-cooled on ice for 1 min. Refolding was initiated by addition of 5 µl ice-cold 10X RNA Folding Buffer [400 mM Tris-HCl pH 7.5; 100 mM $MgCl_2$; 4 mM Spermidine], followed by incubation at 32°C for 5 min. For experiments involving MTX (10 µM final) and/or excess GTP (5 mM final), these were added together with the folding buffer. DMS (from a 1:4 dilution in 100% ethanol) was added at a final concentration of 100 mM, followed by incubation at 32°C for 2 min. Reactions were quenched by addition of 1 volume 1 M DTT, and RNA was purified on Monarch® Spin RNA Cleanup columns (10 µg) as per manufacturer instructions. To prevent carryover of other species that might have formed during the folding/splicing process, the probed RNA was further resolved on a 5% TBE-Urea polyacrylamide gel. The product corresponding to the full-length unspliced RNA was excised and

recovered by passive diffusion at 4°C for 16 h in 300 µl 0.05% SDS, supplemented with 60 U SUPERase•In™ RNase Inhibitor. The same conditions were used for probing of *E. coli* total RNA, that was used for the derivation of optimized folding parameters (see paragraph "*Optimization of folding parameters*" below), except for the folding buffer that was supplemented with 1.5 M KCl, and the temperature of the denaturation step that was increased to 95°C to ensure proper denaturation of the rRNAs.

DMS-MaPseq library preparation of the T4 *td* intron.

For DMS-MaPseq library preparation, 5.25 µl DMS-probed RNA were mixed with 1 µl RT3 primer (Supplementary Data 6) and 1 µl dNTPs (10 mM each), and incubated at 70°C for 5 min, followed by snap-cooling on ice for 1 min. Reactions were then supplemented with 0.5 µl Induro® Reverse Transcriptase (cat. M0681L, New England Biolabs), 0.25 µl SUPERase•In™ RNase Inhibitor, 2 µl 5X RT Buffer [250 mM Tris-HCl pH 8.3; 375 mM KCl; 15 mM $MgCl_2$], and reverse transcription was carried out by incubation at 42°C for 5 min, 55°C for 30 min, 60°C for 30 min and 75°C for 15 min. The Induro-RNA-cDNA complex was destroyed by addition of 1 µl 10 M NaOH, followed by incubation at 95°C for 3 min. Reactions were cleaned up on Monarch® Spin RNA Cleanup columns. cDNA was eluted in 7.5 µl nuclease-free water and mixed with 2.5 µl 1 µM F3 primer (Supplementary Data 6), 2.5 µl 10 µM i5 primer, 2.5 µl 10 µM i7 primer and 12.5 µl NEBNext® Ultra™ II Q5® Master Mix. PCR enrichment was performed as per manufacturer instructions. Amplified libraries were purified using 1 volume NucleoMag NGS Clean-up and Size Select beads.

SHAPE-MaP library preparation.

For SHAPE-MaP library preparation, ~50 ng poly(A)+ RNA, enriched using Oligo d(T)25 Magnetic Beads (cat. S1419S, New England Biolabs), were directly eluted from the beads by fragmentation in 4 mM $MgCl_2$ for 5.5 min at 94°C, and then cleaned up on Monarch® Spin RNA Cleanup columns. The remainder of the protocol was performed as previously described[103] (paragraph 4.3, "Traditional method").

Targeted SHAPE-MaP library preparation.

For targeted SHAPE-MaP across increasing MTX concentrations, 5 µg total RNA were subjected to reverse transcription in a final volume of 20 µl, in the presence of 4 µl RT Buffer 5X [250 mM Tris pH 8.0; 375 mM KCl], 2 µl DTT 0.1 M, 2 µl 10 µM equimolar pool of reverse primers containing the reverse complement of the Illumina 3′ adapter (Supplementary Data 6), 1 µl dNTPs (10 mM each), 200 U SuperScript™ II Reverse Transcriptase and 10 U SUPERase•In™ RNase Inhibitor, by incubating at 42°C for 1h30m, followed by 10 min at 50°C, 10 min at 55°C, and 10 min at 60°C. The reverse transcription reactions were cleaned up Monarch® Spin RNA Cleanup columns and eluted in 20 µl nuclease-free water. Targeted PCR was performed using 2.5 µl cDNA, Phusion™ High-Fidelity DNA Polymerase (cat. M0530L, New England Biolabs), 0.5 µM final of the gene-specific reverse primer (the same used for reverse transcription), 0.5 µM final of the gene-specific forward primer containing the Illumina 5′ adapter (Supplementary Data 6), and a touchdown protocol. Briefly, the annealing temperature was set at 63°C and decreased by -0.5°C/cycle for the first 10 cycles, followed by 20 cycles at 58°C. The purified amplicons were

then equimolarly pooled, and 5 ng of this pool were used for barcoding using barcoded Illumina primers.

5′UTR-MaP library preparation.

5′UTR-MaP library preparation was performed as previously described[120], with minor changes. Briefly, ~1.5 µg of poly(A)+ RNA were enriched per sample using Oligo $d(T)_{25}$ Magnetic Beads and directly eluted from the beads by fragmentation in 4 mM $MgCl_2$ for 5 min at 94°C, and then cleaned up on Monarch® Spin RNA Cleanup columns. RNA was end-repaired in two steps. First, RNA was treated with 1 U Shrimp Alkaline Phosphatase (rSAP) (cat. M0371L, New England Biolabs), in a final volume of 20 µl, at 37°C for 30 min, followed by cleanup on Monarch® Spin RNA Cleanup columns. Then, decapping was performed at 37°C for 1 h, in a final volume of 20 µl, using 5 U Cap-Clip™ Acid Pyrophosphatase (cat. C-CC15011H, CellScript), followed by clean up on Monarch® Spin RNA Cleanup columns. End-repaired RNA fragments were ligated to 1 µl of 10 µM 5′-biotin-TEG-modified RA1 RNA adapter (Supplementary Data 6) at 25°C for 2 h, in a final volume of 20 µl, using 30 U T4 RNA Ligase 1 (ssRNA Ligase), High Concentration (cat. M0437M, New England Biolabs), in T4 RNA Ligase Reaction Buffer supplemented with 12.5% PEG-8000 and 1 mM ATP final. 20 µl Dynabeads™ MyOne™ Streptavidin T1 beads (cat. 65601, ThermoFisher Scientific) were then washed twice in 100 µl 2X Binding & Wash Buffer [10 mM Tris-HCl pH 7.5; 1 mM EDTA; 2 M NaCl] and resuspended in 40 µl of the same buffer. Ligation reactions were then brought to a final volume of 40 µl with nuclease-free water and mixed with the beads. Samples were thoroughly vortexed, then incubated for 15 min at 22°C with constant shaking at 1,000 RPM. Beads were washed twice with 500 µl 1X Binding & Wash Buffer, followed by two washes with 500 µl nuclease-free water at 80°C for 2 min, to remove non-specifically captured RNA fragments. RNA was eluted from the beads in 50 µl Formamide Elution Buffer [95% Formamide; 10 mM EDTA], by incubating at 95°C for 3 min, then cleaned up on Monarch® Spin RNA Cleanup columns. RNA was then ligated to 1 µl of a 10 µM dilution of 5′-pre-adenylated and C3 spacer 3′-blocked DNA 3′ adapter DA1 (Supplementary Data 6), at 25°C for 2 h, in a final volume of 20 µl, using 200 U T4 RNA Ligase 2, truncated KQ (cat. M0373L, New England Biolabs), in T4 RNA Ligase Reaction Buffer supplemented with 12.5% PEG-8000. Ligated RNA was cleaned up on Monarch® Spin RNA Cleanup columns and eluted in 9 µl nuclease-free water, supplemented with 2 µl 10 µM RT primer and 2 µl 10 mM dNTPs. RNA was incubated at 70°C for 5 min, and then snap-cooled on ice for 1 min. Reverse transcription was conducted in a final volume of 20 µl, containing 4 µl 5X RT Buffer [250 mM Tris-HCl pH 8.3; 375 mM KCl; 15 mM $MgCl_2$], 1 µl DTT 0.1 M, 20 U SUPERase•In™ RNase Inhibitor, 200 U Induro® Reverse Transcriptase, and incubated 10 min at 42°C, 1 h at 57°C and 1 h at 60°C. RNA was degraded by addition of 1 µl 10 M NaOH, followed by incubation at 95°C for 3 min. Reactions were cleaned up on Monarch® Spin RNA Cleanup columns, using 1 volume RNA Binding Buffer and 1 volume 100% ethanol, to only recover fragments ≥ 200 nt. The final PCR enrichment was performed using the NEBNext® Ultra™ II Q5® Master Mix (cat. M0544X, New England Biolabs), as per manufacturer instructions.

Ribosome profiling via RiboLace technology.

Ribosome profiling was performed using the RiboLace Pro kit (cat. #RL00P-12, IMMAGINA Biotechnology), with minor changes to the protocol. Briefly, ~7.5 x 10^6 cells were treated with 10

μM final MTX, or an equivalent amount of DMSO, for 30 min at 37°C (see paragraph "*Cell culture and in vivo probing*" above). During the final 5 min of incubation, cycloheximide (CHX) (cat. C4859, Merck) was added at a final concentration of 10 μg/mL. Cells were then washed twice with ice-cold PBS, supplemented with 10 μg/mL CHX, after which the plate was immediately snap-frozen in liquid nitrogen. Cells were then scraped in 300 μl ice-cold SLB, lysed on ice for 20 min and cell debris was removed by centrifugation at 17,000g x 15 min (4°C). Then, 0.55 AU (260 nm) of lysate were digested with 16.5 μl diluted nuclease (dNux) and used for the capture of ribosome-protected fragments (RPF). After the capture, RPFs were directly collected by resuspending the beads in 1 mL TRIzol™ Reagent and by incubating at 70°C for 5 min, followed by RNA extraction as per manufacturer instructions. RPF were end-repaired by treatment with 1 U rSAP, in a final volume of 20 μl, at 37°C for 30 min, followed by heat inactivation of the enzyme at 70°C for 5 min. Reactions were then supplemented with 20 U T4 Polynucleotide Kinase (cat. M0201L, New England Biolabs), 1 mM ATP, 5 mM DTT, in a final volume of 50 μl, and incubated at 37°C for 1 h. 5′-phosphorylated RNA fragments were then cleaned up on Monarch® Spin RNA Cleanup columns, by only recovering fragments < 200 nt. Purified RFP were then subjected to adapter ligation, reverse transcription and PCR following the same procedure used for SHAPE-MaP library preparation, but performing the reverse transcription reaction using 200 U Induro® Reverse Transcriptase.

For RNA-seq library preparation, 100 μl were taken from the remainder of the lysate, mixed with 1 mL ice-cold TRIzol™ Reagent and extracted as per manufacturer instructions. 5 μg total RNA were subjected to poly(A)+ enrichment using Oligo d(T)25 Magnetic Beads and directly eluted from the beads by fragmentation in 4 mM $MgCl_2$ for 8 min at 94°C, and then cleaned up on Monarch® Spin RNA Cleanup columns. Library preparation was performed using the NEBNext® Ultra™ II Directional RNA Library Prep Kit for Illumina® (cat. E7760S, New England Biolabs), as per manufacturer instructions.

Analysis of % splicing efficiencies from sequencing data.

Calculation of % splicing efficiencies from sequencing data was performed using an alignment-free approach. Briefly, a regular expression was defined for either the spliced (TTTCTTGGGTCTTCCATTTA for T4 *td*, CTATGACTCTCTTAAGGTAG for *C. albicans* 25S rRNA) or unspliced (TTTCTTGGGTTAATTGAGGC for T4 *td*, CTATGACTCTCAACCTATAA for *C. albicans* 25S rRNA) RNAs, by taking the last 10 nt of exon 1 and either the first 10 nt of exon 2, or the first 10 nt of the intron. The regular expression was further expanded to allow any 1 nt mismatch. The number of matches for both regular expressions was then calculated for each FASTQ file and the % spliced RNA was calculated as:

$$\%\ spliced = \frac{\#\ spliced\ reads}{\#\ spliced\ reads + \#\ unspliced\ reads} \quad (1)$$

The % spliced relative to control was then calculated by dividing all values by the % splicing efficiency in the control experiment (0 μM MTX). For dose-response experiments, these values were used to derive IC_{50} values using a 4-parameter log-logistic model.

Quantitative Structure-Activity Relationship (QSAR) analysis.

For QSAR analysis, % splicing inhibition was first calculated for all tested anthraquinone compounds, for both T4 *td* and *C. albicans* 25S rRNA introns. After individually averaging the two replicates for each intron, the average % splicing inhibition across both introns was calculated and correlated to all the molecular descriptors available in the RDKit v2025.03.2.

Processing of T4 *td* intron DMS-MaPseq data.

Paired-end reads were clipped of sequencing adapters using Cutadapt[130] v4.478 (parameters: *-A AGATCGGAAG -a AGATCGGAAG -m 200:200 -O 1*) and merged using PEAR[131] v0.9.1179 (parameters: *-n 200 -q 20 -u 0 -e -y 15G -z*). Merged reads were then mapped to the T4 *td* intron sequence using the *rf-map* module of the RNA Framework[132] v2.9.3 and Bowtie2[133] v2.3.5.1 (parameters: *-b2 -ctn -cmn 0 -mp "--very-sensitive-local --norc" -cl 200*). Bulk (ensemble average) mutation counts and coverage (RC files) and MM files (necessary for ensemble deconvolution analysis) were obtained from BAM alignments files using the *rf-count* module of the RNA Framework (parameters: *-m -ds 250 -ncl -es -ni -na -me 0.1 -dc 3 -mm*). Reads harboring more than 10% mutated bases, as well as reads spanning less than 250 nt, were discarded. Insertions, ambiguous deletions and consecutive mutations falling within 3 nt from each other were discarded. Furthermore, a mask file (parameter: *-mf*) was provided to mask the RT primer binding site (TAACGACCTTATCTGAACATAATG). Prior to ensemble deconvolution analysis, MM files were further polished by removing non-A/C mutations and by discarding reads carrying fewer than 2 A/C mutations, by using the *extract* function of the *rf-mmtools* tool of the RNA Framework (parameters: *-mpr 2 -kb AC*).

For the analysis of bulk (ensemble average) data, cross-experiment normalization factors were derived using the *rf-normfactor* utility of the RNA Framework (parameters: *-sm 4 -nm 3 -rb AC -mc 1000*) and provided to the *rf-norm* utility via the *-nf* parameter. Reactivities from independent replicates were combined using the *rf-combine* tool of the RNA Framework. Areas under the Receiver Operator Characteristic (ROC) curve (related to Fig. 3a) were calculated using the T4 *td* intron reference structure, combined reactivities and the *rf-eval* tool of the RNA Framework, by ignoring terminal base-pairs (parameters: *-kl -kp -it*).

Processing of transcriptome-wide SHAPE-MaP data.

Paired-end reads were clipped of sequencing adapters using Cutadapt v4.478 (parameters: *-A AGATCGGAAG -a AGATCGGAAG -m 50:50 -O 1*) and merged using PEAR v0.9.1179 (parameters: *-n 50 -q 20 -u 0 -e -y 15G -z*). Merged reads were then combined with R1 and the reverse-complemented R2 for read pairs that could not be merged, and mapped to the hg38 assembly of the human reference genome using STAR[134] v2.7.10b (parameters: *--outFilterMultimapNmax 10 --alignSJoverhangMin 8 --alignSJDBoverhangMin 2 --outFilterMismatchNmax 999 --outFilterMismatchNoverReadLmax 0.15 --alignIntronMin 20 --alignIntronMax 1000000 --alignMatesGapMax 1000000 --alignEndsType Local --outFilterScoreMinOverLread 0.15 --outFilterMatchNminOverLread 0.15 --outSAMprimaryFlag AllBestScore --outSAMattributes All*). Genome-level mutation counts and coverage (RC files) were obtained from BAM alignments using the *rf-count-genome* module of the RNA Framework (parameters: *-ls second -m -ds 50 -rd -me 0.1 -ncl*). Transcriptome-level counts and coverage were then extracted from genome-level RC files through the *extract* function of the *rf-rctools* utility of the RNA Framework, using the MANE v1.4 gene annotation. For reactivity normalization, cross-

experiment transcriptome-wide normalization factors were derived using the *rf-normfactor* utility of the RNA Framework (parameters: *-sm 3 -nm 3 -mc 1000*) and provided to the *rf-norm* utility via the *-nf* parameter. Only bases with a coverage ≥ 1,000X were retained for downstream analyses.

Identification of MTX-induced reactivity changes from SHAPE-MaP data.

To identify bases (de)protected upon MTX treatment from SHAPE-MaP data, cross-experiment comparison of normalized reactivities was performed for bases having sufficient coverage (≥ 1,000X) across all experiments (2x DMSO-treated cells and 2x MTX-treated cells). In total, each base was subjected to 4 comparisons (MTX, rep. #1 vs. DMSO, rep. #1; MTX, rep. #1 vs. DMSO, rep. #2; MTX, rep. #2 vs. DMSO, rep. #1; MTX, rep. #2 vs. DMSO, rep. #2). The reactivity fold change (FC) for a base *i* was calculated as:

$$FC_i = log_2\left(\frac{M_i + p}{D_i + p}\right) \quad (2)$$

where M_i and D_i are respectively the normalized reactivities of base *i* in the MTX-treated and DMSO-treated samples, while *p* is a pseudocount (0.001) introduced to avoid division by 0. To call a base as (de)protected, the FC for all 4 comparisons had to be ≥ $\log_2(2)$ (deprotection) or ≤ $\log_2(0.5)$ (protection) and the absolute reactivity difference for all 4 comparisons had to be ≥ 0.1 (to reduce noise due to minor fluctuations in SHAPE reactivities). Bases for which the FC for all 4 comparisons was > $\log_2(0.5)$ and < $\log_2(2)$, or the absolute reactivity difference for all 4 comparisons was < 0.1, were considered to be unchanged. The procedure has been implemented in the *diffShape* script (available from the repository https://github.com/dincarnato/papers). Base enrichment analysis (related to Fig. 4c and Supplementary Fig. 13b) was conducted by performing a binomial test for each base, with *x* being the number of times a given base was (de)protected, *n* being the total number of (de)protected bases, and *p* being the background frequency of that base across all the covered bases. Gini index and median reactivity (related to Fig. 4f) were calculated in 5 nt windows centered on (de)protected bases.

To identify regions undergoing changes in SHAPE reactivity upon MTX treatment, a window of increasingly larger size (10, 20, 30, 40 and 50 nt) was slid along each transcript and the Pearson correlation coefficient (PCC) was calculated for each window between the two replicates of DMSO-treated cells or the two replicates of MTX-treated cells. For PCC calculation reactivities were capped at 1.5. For each window size this analysis yielded a distribution of PCCs. The similarity threshold (*S*) was set as the median of the distribution, while the dissimilarity threshold (*D*) was set as the 25th percentile of the distribution. Structurally-disrupted windows were then defined as those windows whose PCCs for all 4 comparisons (MTX, rep. #1 vs. DMSO, rep. #1; MTX, rep. #1 vs. DMSO, rep. #2; MTX, rep. #2 vs. DMSO, rep. #1; MTX, rep. #2 vs. DMSO, rep. #2) were ≤ *D*. Conversely, unchanged windows were defined as those windows whose PCCs for all 4 comparisons were ≥ *S*. Windows of all sizes passing the threshold were then combined into a final non-redundant set and further enlarged by ± 10 nt to include surrounding bases that might have barely failed to pass the selection thresholds. The procedure has been implemented in the *diffShape* script (available from the repository https://github.com/dincarnato/papers).

Processing of 5′UTR-MaP data.

Paired-end reads were clipped of sequencing adapters using Cutadapt v4.478 (parameters: *-A AGATCGGAAG -a AGATCGGAAG -m 75:75 -O 1*) and merged using PEAR v0.9.1179 (parameters: *-n 75 -q 20 -u 0 -e -y 15G -z*). Merged reads were then combined with R1 and the reverse-complemented R2 for read pairs that could not be merged and mapped to a transcriptome reference built on the MANE v1.4 annotation (plus the 18S and 28S rRNA sequences) using the *rf-map* tool of the RNA Framework and Bowtie2 (parameters: *-b2 -cq5 20 -ctn -cmn 0 -mp "--very-sensitive-local" -bnr*). Bulk (ensemble average) mutation counts and coverage (RC files) and MM files (necessary for ensemble deconvolution analysis) were obtained from BAM alignments files using the *rf-count* module of the RNA Framework (parameters: *-m -mm -wl 2000 -ds 100 -es -na -ni -md 1 -dc 3 -me 0.1*). Prior to ensemble deconvolution analysis, MM files were further polished by extracting the sole 5′ UTR + 100 nt of CDS, by removing non-A/C mutations and by discarding reads encompassing less than 90 nt and carrying fewer than 2 A/C mutations, by using the *extract* function of the *rf-mmtools* tool of the RNA Framework (parameters: *-mrl 90 -mpr 2 -kb AC*).

Ensemble deconvolution analysis.

Ensemble deconvolution was performed using the DRACO algorithm[51]. Briefly, DRACO operates by sliding a window of user-defined length along each transcript, keeping only those reads that are fully contained within the window. Within each window, a graph is constructed using co-mutation data: each mutation in a read is treated as a vertex, and mutations that co-occur within the same read are connected by edges. Then, the normalized Laplacian of the graph's adjacency matrix undergoes eigen decomposition and eigengap analysis to estimate the number of distinct RNA conformations present. This estimated number guides a soft partitioning of the graph (via graph-cut), allowing the reconstruction of the individual reactivity profiles for each conformation, along with their relative proportions. Typically, this analysis is performed independently over the different experiments. One of the risks of this approach is that the identified set of weights might only represent a local minimum of the graph-cut score (or a graph-cut score which is optimal only for the specific sample being analyzed), potentially leading to inconsistent conformation reconstruction across replicates. To address this issue, we modified the DRACO algorithm (available as v1.3 from the repository https://github.com/dincarnato/draco/) in such a way that the full information derived from multiple replicates is considered to achieve the best possible graph partitioning, hence ensuring unbiased conformation reconstruction. To this end: 1) Multiple MM files, corresponding to independent replicates are simultaneously imported by DRACO and mutation filtering is performed simultaneously on reads across all replicates, ensuring the generation of graphs sharing the same vertices. Eigen decomposition and eigengap analysis is still performed independently over each of the normalized Laplacians of the adjacency matrices, and the median of the number of conformations identified across the various replicates is used as the true number of clusters. 2) The graph-cut score is minimized simultaneously across all replicates. As the graph-cut score is essentially calculated as the sum of the weights across all vertices for all clusters, when multiple replicates are present the final graph-cut score is simply the sum of the individual graph-cut scores across the graphs of each replicate. As this new implementation of DRACO expects MM files from individual replicates to contain the same transcripts and in the same exact order, we further implemented the *alignIds* function within the *rf-mmtools* utility of the RNA Framework. This takes a set of MM files as input, corresponding to replicate experiments, and outputs a set of MM files containing only the transcripts common to all

replicates. Furthermore, we made two additional improvements. Firstly, from inspection of transcriptome-wide datasets, we noticed that, at times, the first and second eigengaps showed inverted behavior (with the first eigengap being higher than, or overlapping with, its null model, and the second eigengap being lower than its null model), hence we modified the eigengap analysis to allow for such situations. Secondly, in the original implementation of DRACO, when two overlapping regions populating a different number of conformations were detected, reads were assigned only to the one in which the majority of the mutations would fall. However, as in some cases this would cause loss of information on certain transcript regions, we allowed the same read to be assigned to all regions it overlapped with, provided that at least two mutations would fall within the region.

For the T4 *td* intron, DRACO analysis was performed with a window size of 240 nt, slid in 1 nt increments, requiring a minimum base coverage of 2,000X and a minimum of 2,000 reads post-filtering to perform the eigen deconvolution, by repeating the graph-cut procedure 100 times, and by discarding reads that could not be non-ambiguously assigned to a single cluster (parameters: *--winLen 240 --winOffset 1 --minBaseCoverage 2000 --minPermutations 10 --maxPermutations 100 --minFilteredReads 2000 --softClusteringIters 100 --softClusteringWeightModule 0.005 --lookaheadEigengaps 0 --softClusteringInits 500 --skipAmbiguousAssignments*).

For human 5′ UTRs the window size was reduced to 90 nt and the number of graph-cut iterations was reduced to 30 (parameters: *--winLen 90 --winOffset 1 --minBaseCoverage 2000 --minPermutations 10 --maxPermutations 100 --minFilteredReads 2000 --softClusteringIters 30 --softClusteringWeightModule 0.005 --lookaheadEigengaps 0 --softClusteringInits 500 --skipAmbiguousAssignments --ignoreFirstEigengap*).

Reconstructed profiles for regions populating 2+ alternative conformations were extracted from DRACO's JSON output files using the *rf-json2rc* tool of the RNA Framework, including 20 extra nucleotides on either side of the regions (parameters: *-i 0.1 -ki -e 20 -ep 0 -ec 0 -cm -ca*). For the comparison of conformation stoichiometries between control and MTX-treated cells, the JSON files from both conditions were simultaneously passed to the *rf-json2rc* tool to match the corresponding conformations.

Optimization of folding parameters.

Optimal slope and intercept parameters were identified by jackknifing, using RNA Framework's *rf-jackknife* (parameters: *-rp '-md 600' -x -m*), ViennaRNA[135] package v2.5.1 and the modified Fowlkes-Mallows index (mFMI) metric[106]. For DMS-MaPseq analysis of *in vitro* refolded T4 *td* intron, optimal slope (5.0) and intercept (-2.2) parameters were simultaneously optimized on bulk DMS data for the T4 *td* intron control experiment, and on data for the *E. coli* 16S and 23S rRNAs, refolded under the same conditions. For transcriptome-wide SHAPE-MaP analysis, optimal slope (2.2) and intercept (-0.2) parameters were optimized on the human 28S rRNA, by combining reads from both replicates of 2A3-probed DMSO-treated cells. For 5′UTR-MaP data, optimal slope (4.6) and intercept (-2) parameters were used as previously determined[120].

Structure modelling and neighboring base-pair enrichment analysis.

For SHAPE-MaP data, normalized reactivities from the two replicates of the DMSO-treated or MTX-treated cells were separately combined using the *rf-combine* tool of the RNA Framework, and combined reactivities were used for structure modelling using the *rf-fold* tool of the RNA

Framework and the ViennaRNA package (parameters: *-sl 2.2 -in -0.2 -md 600*). Neighboring base-pair enrichment analysis (related to Fig. 4d and Supplementary Fig. 13c) was performed as it follows. Briefly, neighboring base-pairs falling within a 5 nt window centered on each base (de)protected upon MTX treatment (see paragraph "*Identification of MTX-induced structural changes from SHAPE-MaP data*" above) were extracted and counted. A 1 nt bulge was allowed on either side of the helix between the two neighboring pairs, therefore a base-pair *i/j* had to be followed by one of *i+1/j-1*, *i+1/j-2* or *i+2/j-1*. Then, all possible neighboring base-pairs falling within the entire length of the transcripts harboring (de)protected sites were extracted to estimate their background frequency. A binomial test was then performed for each neighboring base-pair, with *x* being the number of times a given neighboring pair was observed within MTX-(de)protected clusters, *n* being the total number neighboring pairs in MTX-(de)protected clusters, and *p* being the background frequency of that neighboring pair.

For 5′UTR-MaP data, normalized reactivities from the two replicates of either DMSO-treated or MTX-treated cells were combined using the *rf-combine* tool, and combined reactivities were used for structure modelling using the *rf-fold* tool (parameters: *-sl 4.6 -in -2*). Neighboring base-pair enrichment analysis (related to Supplementary Fig. 16b) was performed as it follows. Briefly, the expected number of neighboring base-pairs (allowing for a 1 nt bulge on either side of the helix) was determined from: (1) structures from regions populating 2+ conformations in both DMSO-treated and MTX-treated cells, for which the conformation stoichiometry differed ≤ 10% between the two conditions, (2) structures from regions populating 2+ conformations only in DMSO-treated cells, excluding the neighboring base-pairs present both in the DMSO ensemble and in the conformation selected upon MTX treatment, and (3) structures from regions populating 2+ conformations only in MTX-treated cells that could be found both in the DMSO and MTX ensembles (mFMI ≥ 0.85). Conversely, the observed number of neighboring base-pairs was determined from: (1) structures from regions populating 2+ conformations in both DMSO-treated and MTX-treated cells, for which the conformation stoichiometry increased ≥ 20% upon MTX treatment, (2) structures from regions populating 2+ conformations only in DMSO-treated cells, and (3) structures from regions populating 2+ conformations only in MTX-treated cells that could be found only in the MTX ensemble (mFMI < 0.65), likely corresponding to novel conformations selected by MTX. Neighboring base-pairs common to more than one conformation were only counted once.

A binomial test was then performed for each neighboring base-pair, with *x* being the number of times a given neighboring pair was observed, *n* being the total number of observed neighboring pairs, and *p* being the expected probability of that neighboring pair.

Processing of ribosome profiling data.

Reads from ribosome profiling libraries were first mapped to a reference containing only human rRNA, tRNA and snoRNA sequences, using the *rf-map* module of the RNA Framework, and Bowtie2 (parameters: *-b2 -mp "--very-sensitive-local –un clean.fastq --norc"*). Reads that failed to align to this reference were then mapped to the MANE v1.4 transcriptome reference using the *rf-map* module and Bowtie[136] v1.3.1 (parameters: *-cp -b5 1 -ba -bc 32000 -mp "—norc"*). For each protein coding transcript, the number of reads mapping to the CDS was then calculated. RNA-seq reads were directly mapped to the MANE reference, but the "*--norc*" parameter was

changed to "*--nofw*" to account for the different strandedness of the ribosome profiling and RNA-seq library preparation protocols.

For both ribosome profiling and RNA-seq data, per-transcript RPKMs were calculated as:

$$RPKM = \frac{C}{NL} \times 1{,}000{,}000 \quad (3)$$

where *C* was the read count for that transcript, *N* was the total number of reads mapped in the experiment, and *L* was the length of the transcript (for RNA-seq) or of the CDS (for ribosome profiling) in kilobases. Translation efficiency (TE) for expressed genes (RPKM ≥ 10; related to Fig. 5e) was then calculated as:

$$TE = \frac{RPKM_{Ribo-seq} + 0.1}{RPKM_{RNA-seq} + 0.1} \quad (4)$$

where 0.1 is a pseudo count added to avoid division by zero. The TE fold change was then calculated as:

$$FC = log_2\left(\frac{TE_{MTX} + 0.1}{TE_{DMSO} + 0.1}\right) \quad (5)$$

Only genes having a window of differential heterogeneity, falling within their 5′ UTR by at least 45 nt (half the window size used for ensemble deconvolution) were retained.

Data Availability:

The data supporting the findings of this study are available from the corresponding authors upon request. Sequencing data have been deposited to the Gene Expression Omnibus (GEO) database, under the accession GSE302505. Raw MM files for analysis with DRACO are available from Zenodo (https://doi.org/10.5281/zenodo.15874381). Additional processed data are available at https://www.incarnatolab.com/datasets/Mitoxantrone_Zhang_2026.php. Source data for the figures and supplementary figures are provided as a Source Data file.

Code Availability:

The source codes of DRACO v1.3, and of the *diffShape* utility are freely available from GitHub, under the GPLv3 license (https://github.com/dincarnato/draco and https://github.com/dincarnato/papers).

References

1. Warner, K. D., Hajdin, C. E. & Weeks, K. M. Principles for targeting RNA with drug-like small molecules. *Nat Rev Drug Discov* **17**, 547–558 (2018).
2. Childs-Disney, J. L. *et al.* Targeting RNA structures with small molecules. *Nat Rev Drug Discov* **21**, 736–762 (2022).
3. Hewitt, W. M., Calabrese, D. R. & Schneekloth, J. S. Evidence for ligandable sites in structured RNA throughout the Protein Data Bank. *Bioorg Med Chem* **27**, 2253–2260 (2019).
4. Veenbaas, S. D., Koehn, J. T., Irving, P. S., Lama, N. N. & Weeks, K. M. Ligand-binding pockets in RNA and where to find them. *Proc Natl Acad Sci U S A* **122**, e2422346122 (2025).
5. Mustoe, A. M., Brooks, C. L. & Al-Hashimi, H. M. Hierarchy of RNA Functional Dynamics. *Annual Review of Biochemistry* **83**, 441–466 (2014).
6. Ganser, L. R., Kelly, M. L., Herschlag, D. & Al-Hashimi, H. M. The roles of structural dynamics in the cellular functions of RNAs. *Nat Rev Mol Cell Biol* **20**, 474–489 (2019).
7. Spitale, R. C. & Incarnato, D. Probing the dynamic RNA structurome and its functions. *Nat Rev Genet* 1–19 (2022) doi:10.1038/s41576-022-00546-w.
8. Bose, R., Saleem, I. & Mustoe, A. M. Causes, functions, and therapeutic possibilities of RNA secondary structure ensembles and alternative states. *Cell Chem Biol* **31**, 17–35 (2024).
9. Bonilla, S. L., Jones, A. N. & Incarnato, D. Structural and biophysical dissection of RNA conformational ensembles. *Current Opinion in Structural Biology* **88**, 102908 (2024).
10. Siegfried, N. A., Busan, S., Rice, G. M., Nelson, J. A. E. & Weeks, K. M. RNA motif discovery by SHAPE and mutational profiling (SHAPE-MaP). *Nat Methods* **11**, 959–965 (2014).
11. Mustoe, A. M. *et al.* Pervasive Regulatory Functions of mRNA Structure Revealed by High-Resolution SHAPE Probing. *Cell* **173**, 181-195.e18 (2018).
12. Manfredonia, I. *et al.* Genome-wide mapping of SARS-CoV-2 RNA structures identifies therapeutically-relevant elements. *Nucleic Acids Res* **48**, 12436–12452 (2020).
13. Sztuba-Solinska, J., Chavez-Calvillo, G. & Cline, S. E. Unveiling the druggable RNA targets and small molecule therapeutics. *Bioorg Med Chem* **27**, 2149–2165 (2019).
14. Juru, A. U., Patwardhan, N. N. & Hargrove, A. E. Understanding the Contributions of Conformational Changes, Thermodynamics, and Kinetics of RNA–Small Molecule Interactions. *ACS Chem Biol* **14**, 824–838 (2019).
15. Ottink, O. M. *et al.* Ligand-induced folding of the guanine-sensing riboswitch is controlled by a combined predetermined induced fit mechanism. *RNA* **13**, 2202–2212 (2007).

16. Noeske, J. *et al.* Interplay of 'induced fit' and preorganization in the ligand induced folding of the aptamer domain of the guanine binding riboswitch. *Nucleic Acids Res* **35**, 572–583 (2007).
17. Vicens, Q., Mondragón, E. & Batey, R. T. Molecular sensing by the aptamer domain of the FMN riboswitch: a general model for ligand binding by conformational selection. *Nucleic Acids Res* **39**, 8586–8598 (2011).
18. Serganov, A. & Nudler, E. A Decade of Riboswitches. *Cell* **152**, 17–24 (2013).
19. Kovachka, S. *et al.* Covalent Probes Reveal Small-Molecule Binding Pockets in Structured RNA and Enable Bioactive Compound Design. *J Am Chem Soc* **147**, 37460–37479 (2025).
20. Ratni, H. *et al.* Discovery of Risdiplam, a Selective Survival of Motor Neuron-2 (SMN2) Gene Splicing Modifier for the Treatment of Spinal Muscular Atrophy (SMA). *J Med Chem* **61**, 6501–6517 (2018).
21. Ishigami, Y. *et al.* Specificity, synergy, and mechanisms of splice-modifying drugs. *Nat Commun* **15**, 1880 (2024).
22. Campagne, S. *et al.* Structural basis of a small molecule targeting RNA for a specific splicing correction. *Nat Chem Biol* **15**, 1191–1198 (2019).
23. Malard, F. *et al.* The diversity of splicing modifiers acting on A-1 bulged 5'-splice sites reveals rules for rational drug design. *Nucleic Acids Res* **52**, 4124–4136 (2024).
24. Childs-Disney, J. L., Wu, M., Pushechnikov, A., Aminova, O. & Disney, M. D. A small molecule microarray platform to select RNA internal loop-ligand interactions. *ACS Chem Biol* **2**, 745–754 (2007).
25. Tran, T. & Disney, M. D. Two-Dimensional Combinatorial Screening (2DCS) of a Bacterial rRNA A-site-like Motif Library: Defining Privileged Asymmetric Internal Loops that Bind Aminoglycosides. *Biochemistry* **49**, 1833–1842 (2010).
26. Balaratnam, S. *et al.* Investigating the NRAS 5′ UTR as a target for small molecules. *Cell Chem Biol* **30**, 643-657.e8 (2023).
27. Sidharthan, V. *et al.* Use of a small molecule microarray screen to identify inhibitors of the catalytic RNA subunit of Methanobrevibacter smithii RNase P. *Nucleic Acids Res* **53**, gkae1190 (2025).
28. Wicks, S. L. & Hargrove, A. E. Fluorescent Indicator Displacement Assays to Identify and Characterize Small Molecule Interactions with RNA. *Methods* **167**, 3–14 (2019).
29. Davila-Calderon, J. *et al.* IRES-targeting small molecule inhibits enterovirus 71 replication via allosteric stabilization of a ternary complex. *Nat Commun* **11**, 4775 (2020).
30. Binas, O. *et al.* 19 F NMR-Based Fragment Screening for 14 Different Biologically Active RNAs and 10 DNA and Protein Counter-Screens. *Chembiochem* **22**, 423–433 (2021).

31. Lundquist, K. P. *et al.* Design, synthesis, and screening of an RNA optimized fluorinated fragment library. *SLAS Discov* **31**, 100215 (2025).
32. Zeller, M. J. *et al.* SHAPE-enabled fragment-based ligand discovery for RNA. *Proceedings of the National Academy of Sciences* **119**, e2122660119 (2022).
33. Rizvi, N. F. *et al.* Discovery of Selective RNA-Binding Small Molecules by Affinity-Selection Mass Spectrometry. *ACS Chem Biol* **13**, 820–831 (2018).
34. Rizvi, N. F. *et al.* Targeting RNA with Small Molecules: Identification of Selective, RNA-Binding Small Molecules Occupying Drug-Like Chemical Space. *SLAS Discov* **25**, 384–396 (2020).
35. Nickbarg, E. B., Spencer, K. B., Mortison, J. D. & Lee, J. T. Targeting RNA with small molecules: lessons learned from Xist RNA. *RNA* **29**, 463–472 (2023).
36. Childs-Disney, J. L. *et al.* A Massively Parallel Selection of Small Molecule-RNA Motif Binding Partners Informs Design of an Antiviral from Sequence. *Chem* **4**, 2384–2404 (2018).
37. Hargrove, A. E. Small molecule-RNA targeting: Starting with the fundamentals. *Chem Commun (Camb)* **56**, 14744–14756 (2020).
38. Donlic, A. *et al.* R-BIND 2.0: An Updated Database of Bioactive RNA-Targeting Small Molecules and Associated RNA Secondary Structures. *ACS Chem Biol* **17**, 1556–1566 (2022).
39. Yazdani, K. *et al.* Machine Learning Informs RNA-Binding Chemical Space. *Angew Chem Int Ed Engl* **62**, e202211358 (2023).
40. Mortison, J. D. *et al.* Tetracyclines Modify Translation by Targeting Key Human rRNA Substructures. *Cell Chem Biol* **25**, 1506-1518.e13 (2018).
41. Velagapudi, S. P., Li, Y. & Disney, M. D. A cross-linking approach to map small molecule-RNA binding sites in cells. *Bioorg Med Chem Lett* **29**, 1532–1536 (2019).
42. Mukherjee, H. *et al.* PEARL-seq: A Photoaffinity Platform for the Analysis of Small Molecule-RNA Interactions. *ACS Chem Biol* **15**, 2374–2381 (2020).
43. Balaratnam, S. *et al.* A chemical probe based on the PreQ1 metabolite enables transcriptome-wide mapping of binding sites. *Nat Commun* **12**, 5856 (2021).
44. Shah, R. *et al.* Photoaffinity enabled transcriptome-wide identification of splice modulating small molecule–RNA binding events in native cells. *RSC Chem Biol* https://doi.org/10.1039/d4cb00266k doi:10.1039/d4cb00266k.
45. Yang, X. *et al.* Mapping small molecule-RNA binding sites via Chem-CLIP synergized with capillary electrophoresis and nanopore sequencing. *Nucleic Acids Res* **53**, gkaf231 (2025).

46. Fang, L. *et al.* Pervasive transcriptome interactions of protein-targeted drugs. *Nat Chem* **15**, 1374–1383 (2023).
47. Yesley, P., Poulladofonou, G., Incarnato, D. & Velema, W. A. Site-Selective Ligand Selection by Mutational Profiling for Covalent RNA Targeting. *Angew Chem Int Ed Engl* **65**, e17243 (2026).
48. Sengupta, A., Rice, G. M. & Weeks, K. M. Single-molecule correlated chemical probing reveals large-scale structural communication in the ribosome and the mechanism of the antibiotic spectinomycin in living cells. *PLoS Biol* **17**, e3000393 (2019).
49. Wang, Y., Parmar, S., Schneekloth, J. S. & Tiwary, P. Interrogating RNA-Small Molecule Interactions with Structure Probing and Artificial Intelligence-Augmented Molecular Simulations. *ACS Cent Sci* **8**, 741–748 (2022).
50. Tomezsko, P. J. *et al.* Determination of RNA structural diversity and its role in HIV-1 RNA splicing. *Nature* **582**, 438–442 (2020).
51. Morandi, E. *et al.* Genome-scale deconvolution of RNA structure ensembles. *Nat Methods* **18**, 249–252 (2021).
52. Olson, S. W. *et al.* Discovery of a large-scale, cell-state-responsive allosteric switch in the 7SK RNA using DANCE-MaP. *Mol Cell* **82**, 1708-1723.e10 (2022).
53. Yang, M. *et al.* In vivo single-molecule analysis reveals COOLAIR RNA structural diversity. *Nature* https://doi.org/10.1038/s41586-022-05135-9 (2022) doi:10.1038/s41586-022-05135-9.
54. Faulds, D., Balfour, J. A., Chrisp, P. & Langtry, H. D. Mitoxantrone. A review of its pharmacodynamic and pharmacokinetic properties, and therapeutic potential in the chemotherapy of cancer. *Drugs* **41**, 400–449 (1991).
55. Chu, F. K., Maley, G. F., Maley, F. & Belfort, M. Intervening sequence in the thymidylate synthase gene of bacteriophage T4. *Proc Natl Acad Sci U S A* **81**, 3049–3053 (1984).
56. Gott, J. M., Shub, D. A. & Belfort, M. Multiple self-splicing introns in bacteriophage T4: evidence from autocatalytic GTP labeling of RNA in vitro. *Cell* **47**, 81–87 (1986).
57. Cech, T. R., Damberger, S. H. & Gutell, R. R. Representation of the secondary and tertiary structure of group I introns. *Nat Struct Biol* **1**, 273–280 (1994).
58. Janes, J. *et al.* The ReFRAME library as a comprehensive drug repurposing library and its application to the treatment of cryptosporidiosis. *Proc Natl Acad Sci U S A* **115**, 10750–10755 (2018).

59. Shortridge, M. D., Vidalala, V. & Varani, G. The kinase inhibitor Palbociclib is a potent and specific RNA-binding molecule. 2022.01.20.477126 Preprint at https://doi.org/10.1101/2022.01.20.477126 (2022).
60. Meyer, S. M. *et al.* Optimization of a Protein-Targeted Medicine into an RNA-Specific Small Molecule. *ACS Chem Biol* **18**, 2336–2342 (2023).
61. von Ahsen, U., Davies, J. & Schroeder, R. Antibiotic inhibition of group I ribozyme function. *Nature* **353**, 368–370 (1991).
62. von Ahsen, U., Davies, J. & Schroeder, R. Non-competitive inhibition of group I intron RNA self-splicing by aminoglycoside antibiotics. *J Mol Biol* **226**, 935–941 (1992).
63. von Ahsen, U. & Noller, H. F. Footprinting the sites of interaction of antibiotics with catalytic group I intron RNA. *Science* **260**, 1500–1503 (1993).
64. Hoch, I., Berens, C., Westhof, E. & Schroeder, R. Antibiotic inhibition of RNA catalysis: neomycin B binds to the catalytic core of the td group I intron displacing essential metal ions. *J Mol Biol* **282**, 557–569 (1998).
65. Mercure, S., Montplaisir, S. & Lemay, G. Correlation between the presence of a self-splicing intron in the 25S rDNA of C.albicans and strains susceptibility to 5-fluorocytosine. *Nucleic Acids Res* **21**, 6020–6027 (1993).
66. Bass, B. L. & Cech, T. R. Ribozyme inhibitors: deoxyguanosine and dideoxyguanosine are competitive inhibitors of self-splicing of the Tetrahymena ribosomal ribonucleic acid precursor. *Biochemistry* **25**, 4473–4477 (1986).
67. Yarus, M. A specific amino acid binding site composed of RNA. *Science* **240**, 1751–1758 (1988).
68. von Ahsen, U. & Schroeder, R. Streptomycin and self-splicing. *Nature* **346**, 801 (1990).
69. von Ahsen, U. & Schroeder, R. Streptomycin inhibits splicing of group I introns by competition with the guanosine substrate. *Nucleic Acids Res* **19**, 2261–2265 (1991).
70. Liu, T. *et al.* Molecular insights into de novo small-molecule recognition by an intron RNA structure. *Proc Natl Acad Sci U S A* **122**, e2502425122 (2025).
71. Pors, K. *et al.* Alchemix: a novel alkylating anthraquinone with potent activity against anthracycline- and cisplatin-resistant ovarian cancer. *Mol Cancer Ther* **2**, 607–610 (2003).
72. Pors, K. *et al.* Synthesis and biological evaluation of novel chloroethylaminoanthraquinones with potent cytotoxic activity against cisplatin-resistant tumor cells. *J Med Chem* **47**, 1856–1859 (2004).

73. Pors, K. *et al.* Synthesis of DNA-directed pyrrolidinyl and piperidinyl confined alkylating chloroalkylaminoanthraquinones: potential for development of tumor-selective N-oxides. *J Med Chem* **49**, 7013–7023 (2006).
74. Abdallah, Q. M. A. *et al.* Minor structural modifications to alchemix influence mechanism of action and pharmacological activity. *Biochem Pharmacol* **83**, 1514–1522 (2012).
75. Wright, E. P. *et al.* Mitoxantrone and Analogues Bind and Stabilize i-Motif Forming DNA Sequences. *Sci Rep* **6**, 39456 (2016).
76. Errington, R. J. *et al.* Probing cytochrome P450 bioactivation and fluorescent properties with morpholinyl-tethered anthraquinones. *Bioorg Med Chem Lett* **28**, 1274–1277 (2018).
77. Sugiura, Y., Shiraki, T., Konishi, M. & Oki, T. DNA intercalation and cleavage of an antitumor antibiotic dynemicin that contains anthracycline and enediyne cores. *Proc Natl Acad Sci U S A* **87**, 3831–3835 (1990).
78. Carlson, C. B., Vuyisich, M., Gooch, B. D. & Beal, P. A. Preferred RNA binding sites for a threading intercalator revealed by in vitro evolution. *Chem Biol* **10**, 663–672 (2003).
79. Zheng, S., Chen, Y., Donahue, C. P., Wolfe, M. S. & Varani, G. Structural basis for stabilization of the tau pre-mRNA splicing regulatory element by novantrone (mitoxantrone). *Chem Biol* **16**, 557–566 (2009).
80. Verebová, V. *et al.* Anthraquinones quinizarin and danthron unwind negatively supercoiled DNA and lengthen linear DNA. *Biochem Biophys Res Commun* **444**, 50–55 (2014).
81. Mohammad, H. *et al.* Role of intercalation in the electrical properties of nucleic acids for use in molecular electronics. *Nanoscale Horiz* **6**, 651–660 (2021).
82. Sosic, A. *et al.* Multifaceted Aspects of HIV-1 Nucleocapsid Inhibition by TAR-Targeting Peptidyl-Anthraquinones Bearing Terminal Aromatic Moieties. *Viruses* **14**, 2133 (2022).
83. Kapuscinski, J. & Darzynkiewicz, Z. Interactions of antitumor agents Ametantrone and Mitoxantrone (Novatrone) with double-stranded DNA. *Biochem Pharmacol* **34**, 4203–4213 (1985).
84. Pommier, Y., Leo, E., Zhang, H. & Marchand, C. DNA Topoisomerases and Their Poisoning by Anticancer and Antibacterial Drugs. *Chem Biol* **17**, 421–433 (2010).
85. Feofanov, A., Sharonov, S., Kudelina, I., Fleury, F. & Nabiev, I. Localization and molecular interactions of mitoxantrone within living K562 cells as probed by confocal spectral imaging analysis. *Biophys J* **73**, 3317–3327 (1997).
86. Gopinath, S. C. B., Matsugami, A., Katahira, M. & Kumar, P. K. R. Human vault-associated non-coding RNAs bind to mitoxantrone, a chemotherapeutic compound. *Nucleic Acids Res* **33**, 4874–4881 (2005).

87. Velagapudi, S. P. *et al.* Approved Anti-Cancer Drugs Target Oncogenic Non-Coding RNAs. *Cell Chem Biol* **25**, 1086-1094.e7 (2018).
88. Zwelling, L. A. *et al.* Activity of two novel anthracene-9,10-diones against human leukemia cells containing intercalator-sensitive or -resistant forms of topoisomerase II. *Biochem Pharmacol* **46**, 265–271 (1993).
89. McKeown, S. R., Hejmadi, M. V., McIntyre, I. A., McAleer, J. J. & Patterson, L. H. AQ4N: an alkylaminoanthraquinone N-oxide showing bioreductive potential and positive interaction with radiation in vivo. *Br J Cancer* **72**, 76–81 (1995).
90. Zubradt, M. *et al.* DMS-MaPseq for genome-wide or targeted RNA structure probing in vivo. *Nat Methods* **14**, 75–82 (2017).
91. Yazdani, K. *et al.* Decoding complexity in biomolecular recognition of DNA i-motifs with microarrays. *Nucleic Acids Res* **51**, 12020–12030 (2023).
92. Liu, T. & Pyle, A. M. Discovery of highly reactive self-splicing group II introns within the mitochondrial genomes of human pathogenic fungi. *Nucleic Acids Res* **49**, 12422–12432 (2021).
93. Walstrum, S. A. & Uhlenbeck, O. C. The self-splicing RNA of Tetrahymena is trapped in a less active conformation by gel purification. *Biochemistry* **29**, 10573–10576 (1990).
94. Zhang, A., Derbyshire, V., Salvo, J. L. & Belfort, M. Escherichia coli protein StpA stimulates self-splicing by promoting RNA assembly in vitro. *RNA* **1**, 783–793 (1995).
95. Pan, J., Thirumalai, D. & Woodson, S. A. Folding of RNA involves parallel pathways. *J Mol Biol* **273**, 7–13 (1997).
96. Treiber, D. K., Rook, M. S., Zarrinkar, P. P. & Williamson, J. R. Kinetic intermediates trapped by native interactions in RNA folding. *Science* **279**, 1943–1946 (1998).
97. Russell, R. & Herschlag, D. Probing the folding landscape of the Tetrahymena ribozyme: commitment to form the native conformation is late in the folding pathway. *J Mol Biol* **308**, 839–851 (2001).
98. Waldsich, C., Masquida, B., Westhof, E. & Schroeder, R. Monitoring intermediate folding states of the td group I intron in vivo. *EMBO J* **21**, 5281–5291 (2002).
99. Sinan, S., Yuan, X. & Russell, R. The Azoarcus group I intron ribozyme misfolds and is accelerated for refolding by ATP-dependent RNA chaperone proteins. *J Biol Chem* **286**, 37304–37312 (2011).
100. Li, S. *et al.* Topological crossing in the misfolded Tetrahymena ribozyme resolved by cryo-EM. *Proc Natl Acad Sci U S A* **119**, e2209146119 (2022).

101. Bonilla, S. L., Vicens, Q. & Kieft, J. S. Cryo-EM reveals an entangled kinetic trap in the folding of a catalytic RNA. *Sci Adv* **8**, eabq4144 (2022).

102. Marinus, T., Fessler, A. B., Ogle, C. A. & Incarnato, D. A novel SHAPE reagent enables the analysis of RNA structure in living cells with unprecedented accuracy. *Nucleic Acids Res* **49**, e34 (2021).

103. Incarnato, D. Sequencing-based analysis of RNA structures in living cells with 2A3 via SHAPE-MaP. *Methods Enzymol* **691**, 153–181 (2023).

104. Burns, C. P., Haugstad, B. N. & North, J. A. Membrane transport of mitoxantrone by L1210 leukemia cells. *Biochem Pharmacol* **36**, 857–860 (1987).

105. Bell, D. H. Characterization of the fluorescence of the antitumor agent, mitoxantrone. *Biochim Biophys Acta* **949**, 132–137 (1988).

106. Lan, T. C. T. *et al.* Secondary structural ensembles of the SARS-CoV-2 RNA genome in infected cells. *Nat Commun* **13**, 1128 (2022).

107. Miglietta, G. *et al.* RNA G-Quadruplexes in Kirsten Ras (KRAS) Oncogene as Targets for Small Molecules Inhibiting Translation. *J Med Chem* **60**, 9448–9461 (2017).

108. Zhao, J. *et al.* Enhanced transcriptome-wide RNA G-quadruplex sequencing for low RNA input samples with rG4-seq 2.0. *BMC Biol* **20**, 257 (2022).

109. Foye, W. O., Vajragupta, O. & Sengupta, S. K. DNA-binding specificity and RNA polymerase inhibitory activity of bis(aminoalkyl)anthraquinones and bis(methylthio)vinylquinolinium iodides. *J Pharm Sci* **71**, 253–257 (1982).

110. Lown, J. W., Hanstock, C. C., Bradley, R. D. & Scraba, D. G. Interactions of the antitumor agents mitoxantrone and bisantrene with deoxyribonucleic acids studied by electron microscopy. *Mol Pharmacol* **25**, 178–184 (1984).

111. Panousis, C. & Phillips, D. R. DNA sequence specificity of mitoxantrone. *Nucleic Acids Res* **22**, 1342–1345 (1994).

112. Parker, B. S., Cutts, S. M., Cullinane, C. & Phillips, D. R. Formaldehyde activation of mitoxantrone yields CpG and CpA specific DNA adducts. *Nucleic Acids Res* **28**, 982–990 (2000).

113. Liaw, Y. C. *et al.* Antitumor drug nogalamycin binds DNA in both grooves simultaneously: molecular structure of nogalamycin-DNA complex. *Biochemistry* **28**, 9913–9918 (1989).

114. Van Nostrand, E. L. *et al.* A large-scale binding and functional map of human RNA-binding proteins. *Nature* **583**, 711–719 (2020).

115. Lambert, N. *et al.* RNA Bind-n-Seq: quantitative assessment of the sequence and structural binding specificity of RNA binding proteins. *Mol Cell* **54**, 887–900 (2014).

116. Orenstein, Y., Ohler, U. & Berger, B. Finding RNA structure in the unstructured RBPome. *BMC Genomics* **19**, 154 (2018).

117. Jolma, A. *et al.* Binding specificities of human RNA-binding proteins toward structured and linear RNA sequences. *Genome Res* **30**, 962–973 (2020).

118. Laverty, K. U. *et al.* PRIESSTESS: interpretable, high-performing models of the sequence and structure preferences of RNA-binding proteins. *Nucleic Acids Res* **50**, e111 (2022).

119. Harris, S. E. *et al.* Dissecting RNA selectivity mediated by tandem RNA-binding domains. *J Biol Chem* **301**, 108435 (2025).

120. Borovská, I. *et al.* Identification of conserved RNA regulatory switches in living cells using RNA secondary structure ensemble mapping and covariation analysis. *Nat Biotechnol* https://doi.org/10.1038/s41587-025-02739-0 (2025) doi:10.1038/s41587-025-02739-0.

121. Clamer, M. *et al.* Active Ribosome Profiling with RiboLace. *Cell Rep* **25**, 1097-1108.e5 (2018).

122. Cohen, S. S. & Lichtenstein, J. Polyamines and ribosome structure. *J Biol Chem* **235**, 2112–2116 (1960).

123. Stevens, L. The binding of spermine to the ribosomes and ribosomal ribonucleic acid from Bacillus stearothermophilus. *Biochem J* **113**, 117–121 (1969).

124. Hardy, S. J. & Turnock, G. Stabilization of 70S ribosomes by spermidine. *Nat New Biol* **229**, 17–19 (1971).

125. Yoshida, M., Kashiwagi, K., Kawai, G., Ishihama, A. & Igarashi, K. Polyamine enhancement of the synthesis of adenylate cyclase at the translational level and the consequential stimulation of the synthesis of the RNA polymerase sigma 28 subunit. *J Biol Chem* **276**, 16289–16295 (2001).

126. Koculi, E., Lee, N.-K., Thirumalai, D. & Woodson, S. A. Folding of the Tetrahymena ribozyme by polyamines: importance of counterion valence and size. *J Mol Biol* **341**, 27–36 (2004).

127. Lightfoot, H. L. & Hall, J. Endogenous polyamine function—the RNA perspective. *Nucleic Acids Res* **42**, 11275–11290 (2014).

128. Neuner, E., Frener, M., Lusser, A. & Micura, R. Superior cellular activities of azido- over amino-functionalized ligands for engineered preQ1 riboswitches in E.coli. *RNA Biol* **15**, 1376–1383 (2018).

129. Sander, T., Freyss, J., von Korff, M. & Rufener, C. DataWarrior: an open-source program for chemistry aware data visualization and analysis. *J Chem Inf Model* **55**, 460–473 (2015).

130. Martin, M. Cutadapt removes adapter sequences from high-throughput sequencing reads. *EMBnet.journal* **17**, 10–12 (2011).

131. Zhang, J., Kobert, K., Flouri, T. & Stamatakis, A. PEAR: a fast and accurate Illumina Paired-End reAd mergeR. *Bioinformatics* **30**, 614–620 (2014).

132. Incarnato, D., Morandi, E., Simon, L. M. & Oliviero, S. RNA Framework: an all-in-one toolkit for the analysis of RNA structures and post-transcriptional modifications. *Nucleic Acids Res* **46**, e97 (2018).

133. Langmead, B. & Salzberg, S. L. Fast gapped-read alignment with Bowtie 2. *Nat Methods* **9**, 357–359 (2012).

134. Dobin, A. *et al.* STAR: ultrafast universal RNA-seq aligner. *Bioinformatics* **29**, 15–21 (2013).

135. Lorenz, R. *et al.* ViennaRNA Package 2.0. *Algorithms Mol Biol* **6**, 26 (2011).

136. Langmead, B., Trapnell, C., Pop, M. & Salzberg, S. L. Ultrafast and memory-efficient alignment of short DNA sequences to the human genome. *Genome Biol* **10**, R25 (2009).

Acknowledgments

This work was supported by grant from the European Research Council (European Union's Horizon Europe research and innovation programme), grant agreement number 101124787 (RNAStrEnD) to D.I, and partly supported by the Intramural Research Program of the National Institutes of Health (NIH) (ZIABC011585). The contributions of the NIH author(s) were made as part of their official duties as NIH federal employees, are in compliance with agency policy requirements, and are considered Works of the United States Government. However, the findings and conclusions presented in this paper are those of the author(s) and do not necessarily reflect the views of the NIH or the U.S. Department of Health and Human Services.

Author contributions

C.Z. and D.I. designed the experiments, with input from J.S.S., K.P. and M.D.W.; C.Z., I.B., T.I., M.S.M.I. and O.S.O. performed the experiments; R.B. performed the microscopy; M.S.N.I., O.S.O., M.D.W. and K.P. performed synthesis and characterization of the anthraquinone analogs; E.M. and D.I. optimized the DRACO algorithm and performed the bioinformatic analyses; M.C. supported the RiboLace analysis; C.Z., I.B., J.S.S. and D.I. wrote the article with input from all the authors; D.I. supervised the research.

Competing interests

M.C. is the founder of, director of, and a shareholder in IMMAGINA Biotechnology S.r.l. The remaining authors declare no competing interests.

Figure legends

Fig. 1. Identification and characterization of Mitoxantrone (MTX) as a group I self-splicing inhibitor. (**a**) Schematic outline of the high-throughput sequencing-based screening platform used to identify small molecule modulators of RNA structure and function. (**b**) Box plot of T4 *td* intron % splicing for different sets of screened compounds, as compared to DMSO-treated control splicing reactions. Boxes span the 25th to the 75th percentile. The center represents the median. Whiskers span between the 25th percentile – 1.5 times the IQR and the 75th percentile + 1.5 times the IQR. P-values were calculated using a one-tailed Wilcoxon rank sum test. For DMSO and Neomycin, the data points represent independent technical replicates, while, for the compound library, each data point corresponds to n = 1 different compounds. (**c**) Bar plot of T4 *td* intron % splicing in the presence of increasing concentrations of MTX. Data points represent n = 2 independent experiments. (**d**) Bar plot of T4 *td* intron % splicing in the presence of an inhibitory concentration of MTX (10 μM) and increasing concentrations of GTP. Data points represent n = 2 independent experiments.

Fig. 2. Quantitative structure-activity relationship (QSAR) analysis of MTX. (**a**) Heatmap of % splicing inhibition of T4 *td* and *C. albicans* 25S rRNA group I introns by MTX and other anthraquinone compounds, across n = 2 independent experiments. Natural anthraquinones are highlighted in green. (**b**) Scatter plot of average % splicing inhibition (measured across n = 2 independent experiments) by MTX and other anthraquinone compounds. Natural anthraquinones are highlighted in green, MTX in purple. (**c**) Bar plot of Pearson correlation coefficients (PCC) between average % splicing inhibition (calculated on both T4 *td* and *C. albicans* 25S rRNA group I introns) and the top-15 positively correlated molecular descriptors. (**d**) Bar plot of % splicing inhibition of T4 *td* and *C. albicans* 25S rRNA group I introns by synthetic Quinizarin analogs, across n = 2 independent experiments.

Fig. 3. Ensemble deconvolution analysis of the T4 *td* group I intron. (**a**) Receiver operating characteristic curve (ROC) analysis of bulk (ensemble average) DMS reactivities for control, MTX-treated and denatured T4 *td* intron. Curves were calculated over reactivity data averaged across n = 3 (for control and MTX) or n = 2 (for denatured) independent experiments The dashed line corresponds to a random prediction. (**b**) Distributions of bulk (ensemble average) DMS reactivities for control, MTX-treated and denatured T4 *td* intron, across paired (blue) and unpaired (purple) bases. P-values were calculated using a one-tailed Wilcoxon rank sum test. (**c**) Ensemble

deconvolution analysis of T4 *td* intron, treated or not with an inhibitory concentration of MTX (10 μM). Average reactivities, standard deviations (error bars) and relative conformation abundances are derived from n = 3 independent experiments. (**d**) Heatmap of pairwise Pearson correlation coefficients between the states composing the control and MTX-treated T4 *td* intron's ensembles.

Fig. 4. Transcriptome-wide SHAPE-MaP analysis of human cells treated with MTX. (**a**) Scatter plot of Gini index difference versus Pearson correlation coefficient (PCC) of raw SHAPE reactivities for DMSO versus MTX-treated cells. Each data point corresponds to a 40 nucleotide-long window. Windows were slid in 20 nucleotide increments. Bases having mutation rate > 0.05 in the non-probed (DMSO) sample, were excluded. Only a random subset of 10% of the data points is shown. For each window, PCC and Gini index values were averaged across all comparisons (DMSO #1 vs. MTX #1, DMSO #1 vs. MTX #2, DMSO #2 vs. MTX #1, and DMSO #2 vs. MTX #2). The box plots represent the distributions of PCC (blue) and Gini index difference (purple) values across the dataset. (**b**) Distribution of modified Fowlkes-Mallows index values calculated in 40 nucleotide-long windows, slid in 20 nucleotide increments, across the transcriptomes of DMSO versus MTX-treated cells. (**c**) Bar plots depicting the enrichment/depletion of bases on sites of differential (de)protection by MTX. P-values were calculated using a two-tailed binomial test. Stars mark significantly enriched/depleted bases. (**d**) Bar plot depicting the enrichment/depletion of neighboring base-pairs in 5 nucleotide-long windows centered on sites of differential (de)protection by MTX. Secondary structure modelling was constrained by SHAPE reactivities from DMSO-treated cells. P-values were calculated using a two-tailed binomial test. Only pairs with $-\log_{10}$(p-value) > 10 are shown. (**e**) Box plot depicting the distribution of distances between each site of differential protection by MTX and its closest neighbor (using sites common to n = 2 biological replicates). (**f**) Box plots depicting the distribution of Gini indexes (left) and median SHAPE reactivities (right) calculated in 5 nucleotide-long windows centered on sites of differential protection by MTX (using sites common to n = 2 biological replicates and excluding windows with < 4 non-NaN values). P-values were calculated using a two-tailed paired Wilcoxon rank sum test. (**g**) Representative profile of an mRNA, depicting the rolling PCC of SHAPE reactivities for DMSO versus MTX-treated cells, calculated in 40 nucleotide-long sliding windows. The green dashed line represents the median PCC along the entire mRNA. Two regions of localized MTX-induced SHAPE reactivity change are shown along with their respective reactivity profiles and modelled secondary structures, in DMSO and MTX-treated cells, from n = 2 biological replicates. For all box plots, boxes span the 25th to the

75th percentile. The center represents the median. Whiskers span between the 25th percentile – 1.5 times the IQR and the 75th percentile + 1.5 times the IQR.

Fig. 5. Modulation of 5′ UTR RNA structural ensembles by MTX. (**a**) Pie charts depicting the percentages of bases populating 1, 2, or 3+ conformations in DMSO and MTX-treated cells. (**b**) Pie chart depicting the percentages of bases (covered in both DMSO and MTX-treated cells) for which the ensemble heterogeneity increases (red), decreases (blue), or remains unchanged (grey) upon MTX treatment. (**c**) Example of a 5′ UTR forming two conformations in DMSO-treated cells, but only one upon MTX treatment. Average reactivities and relative conformation abundances are derived from n = 2 biological replicates. (**d**) Scatter plots comparing the relative conformation abundances for regions found to populate 2+ conformations both in DMSO and MTX-treated cells. (**e**) Box plot depicting the $\log_2$ fold change in translation efficiency (TE) calculated between MTX versus DMSO-treated cells, for genes whose 5′ UTRs encompassed regions of differential structural heterogeneity upon MTX treatment, as compared to genes whose structural heterogeneity did not change (grey). P-values were calculated using a two-tailed Wilcoxon rank sum test. TEs were averaged across n = 2 biological replicates. Boxes span the 25th to the 75th percentile. The center represents the median. Whiskers span between the 25th percentile – 1.5 times the IQR and the 75th percentile + 1.5 times the IQR.

Editorial Summary:
Mitoxantrone is an FDA-approved anticancer drug that also acts as a general inhibitor of group I intron self-splicing. Here the authors show that Mitoxantrone repartitions RNA conformational ensembles rather than simply binding RNA, stabilizing specific GC-rich structures. This reduces 5' UTR heterogeneity and increases translation efficiency.
Peer review information: *Nature Communications* thanks Yiliang Ding, and the other, anonymous, reviewer(s) for their contribution to the peer review of this work. A peer review file is available.

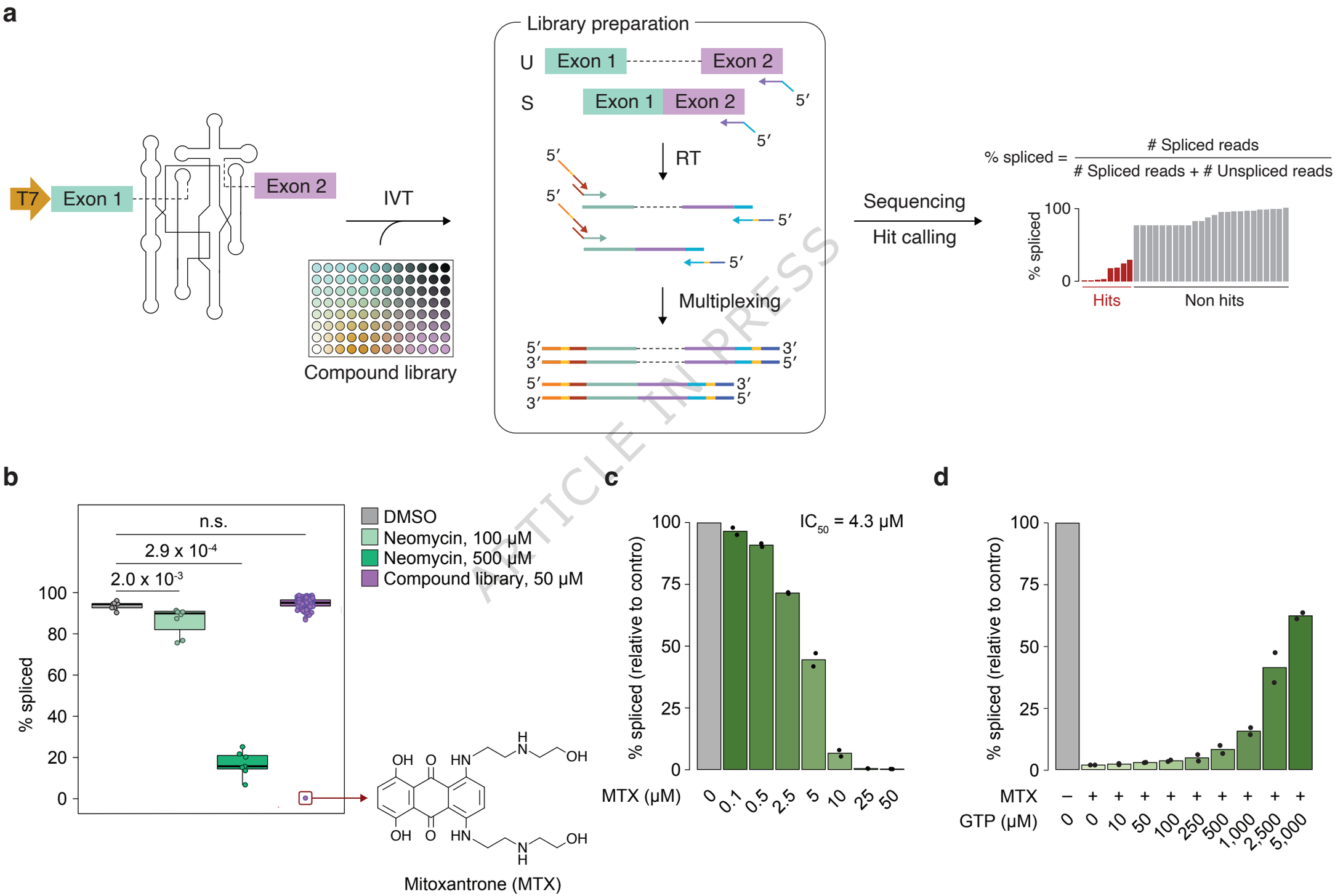

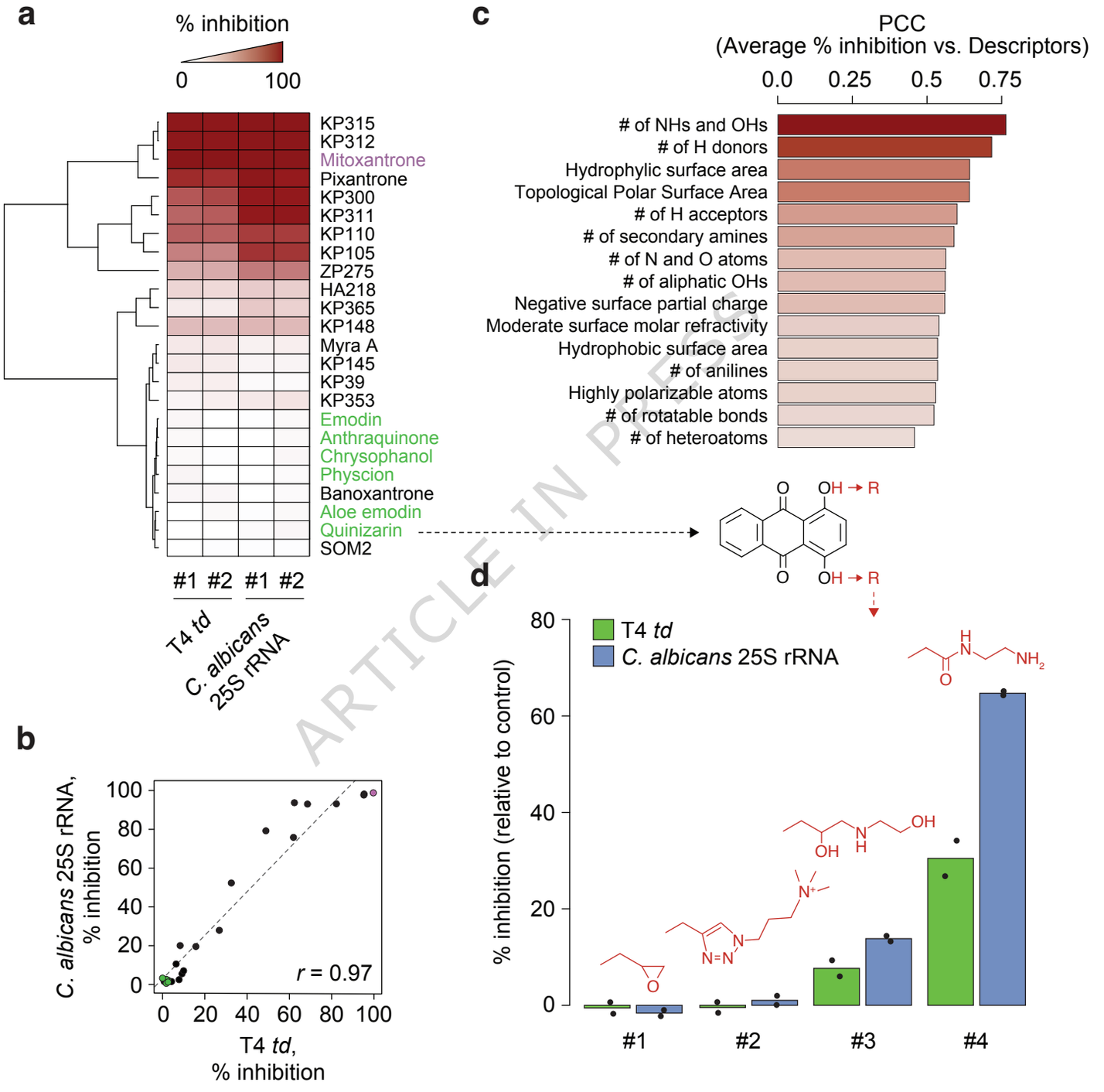

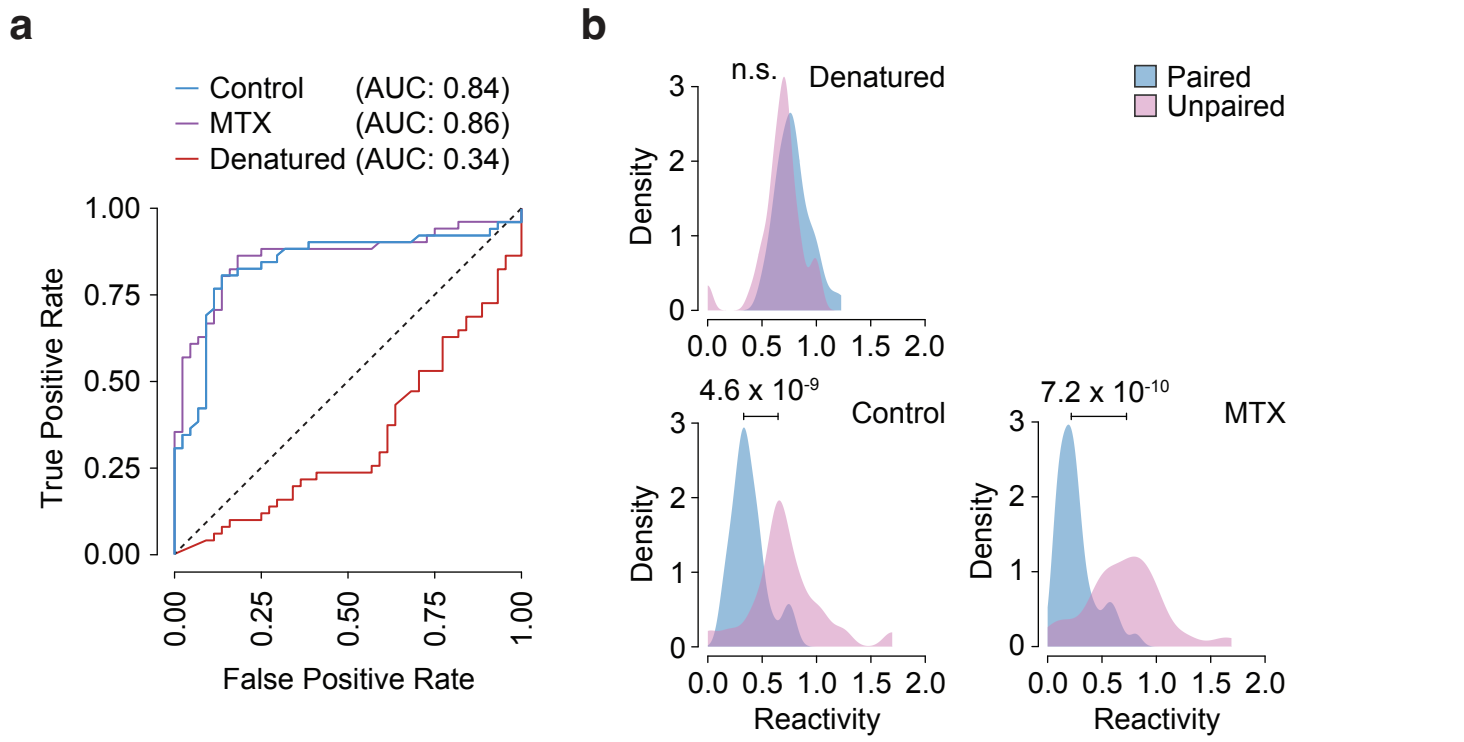
a
Control (AUC: 0.84)
MTX (AUC: 0.86)
Denatured (AUC: 0.34)
True Positive Rate
False Positive Rate
b
n.s.
Denatured
Paired
Unpaired
4.6 x 10-9
Control
7.2 x 10-10
MTX
Density
Reactivity
c
Control, State A (63.2 ± 0.95%)
Control, State B (36.8 ± 0.95%)
MTX, State A (100%)
Reactivity
Base-pair probability
React.
d
MTX #3, State A
MTX #2, State A
MTX #1, State A
Ctrl #2, State A
Ctrl #1, State A
Ctrl #3, State A
Ctrl #3, State B
Ctrl #1, State B
Ctrl #2, State B
PCC

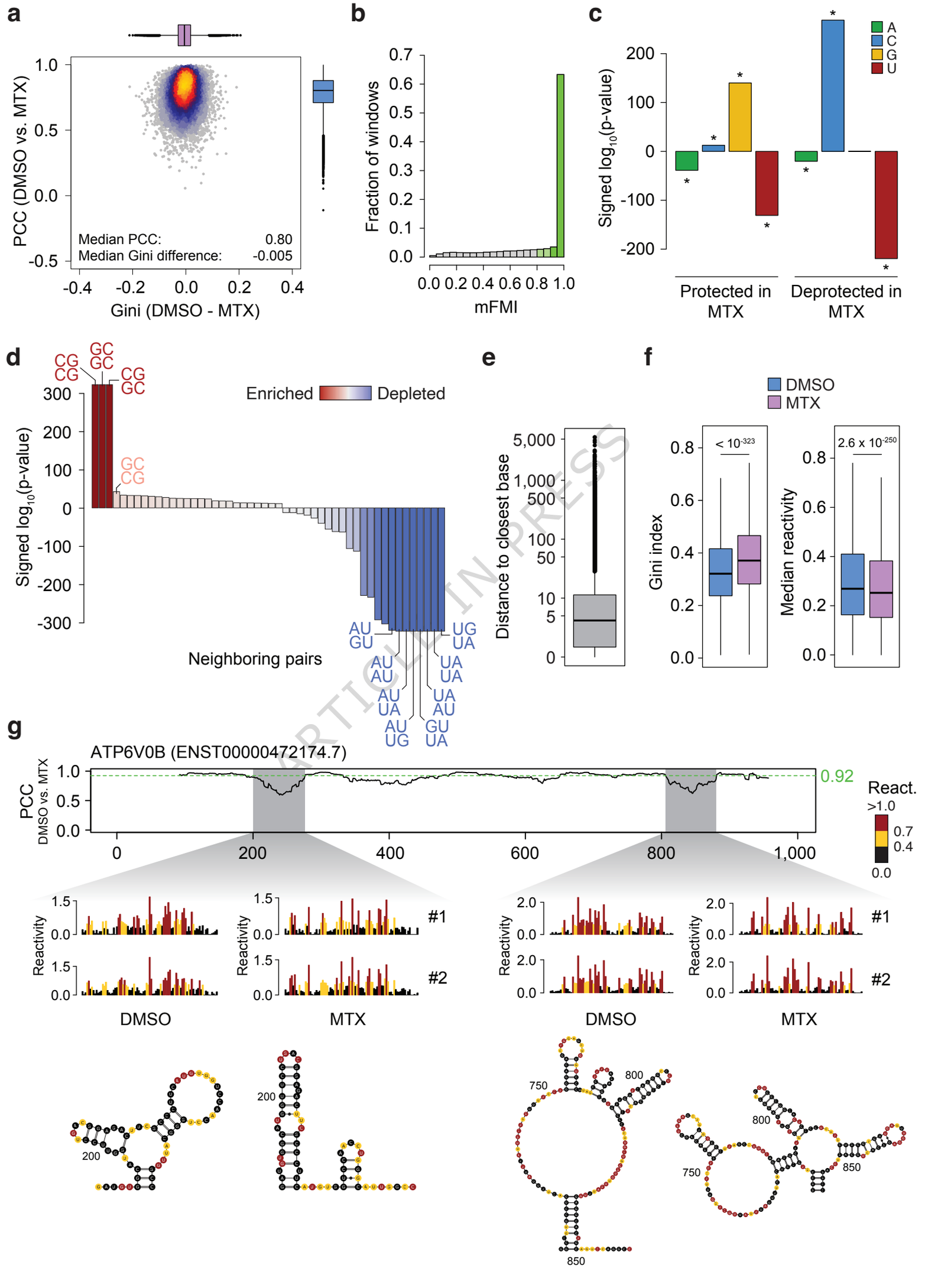
a
PCC (DMSO vs. MTX)
Gini (DMSO - MTX)
Median PCC: 0.80
Median Gini difference: -0.005
b
Fraction of windows
mFMI
c
Signed log10(p-value)
A
C
G
U
Protected in MTX
Deprotected in MTX
d
Enriched
Depleted
Signed log10(p-value)
Neighboring pairs
e
Distance to closest base
f
DMSO
MTX
Gini index
Median reactivity
< 10-323
2.6 x 10-250
g
ATP6V0B (ENST00000472174.7)
PCC DMSO vs. MTX
0.92
React.
>1.0
Reactivity
#1
#2
DMSO
MTX

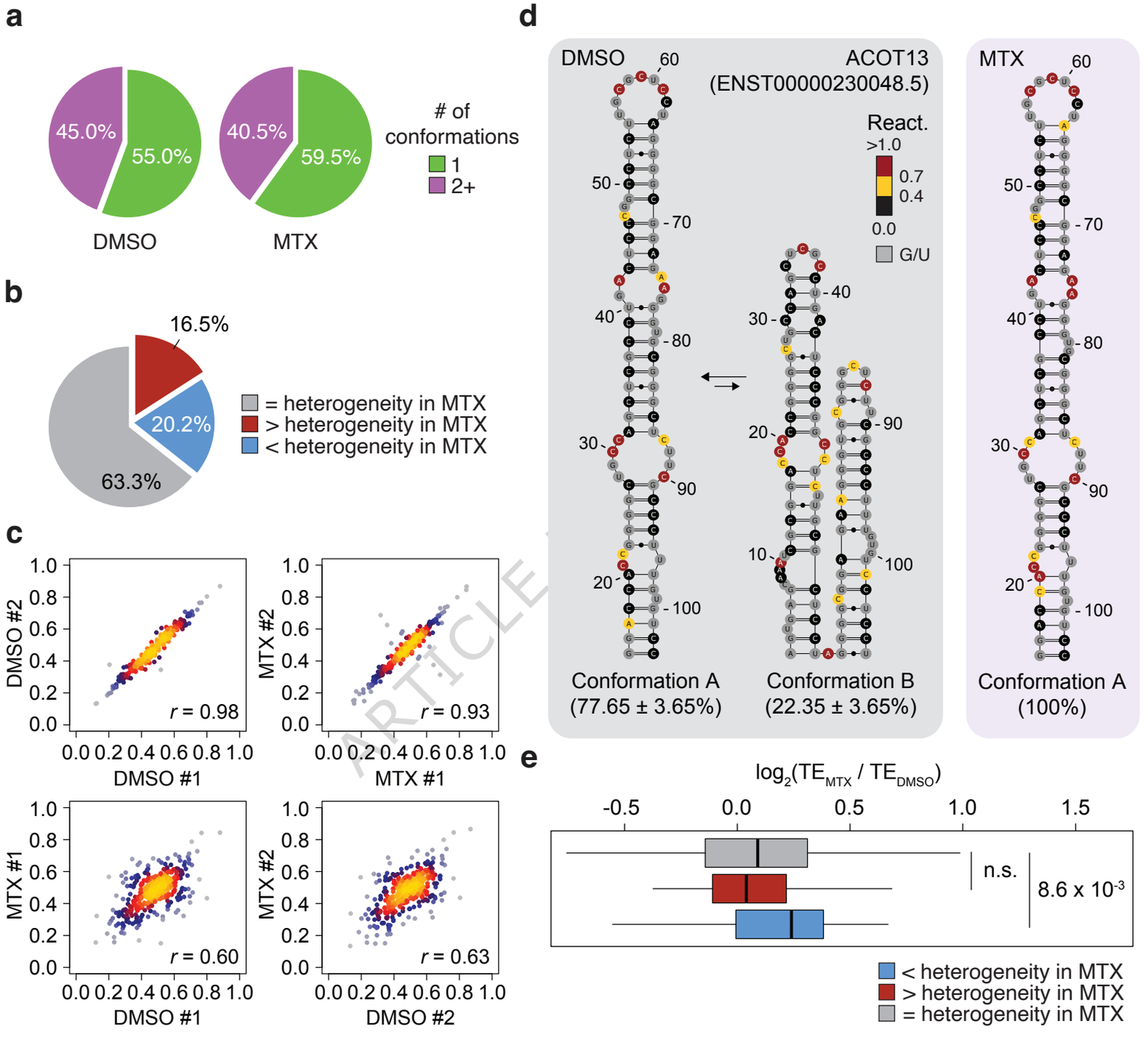
a
45.0%
55.0%
40.5%
59.5%
DMSO
MTX
# of conformations
1
2+
b
16.5%
20.2%
63.3%
= heterogeneity in MTX
> heterogeneity in MTX
< heterogeneity in MTX
c
DMSO #2
DMSO #1
r = 0.98
MTX #2
MTX #1
r = 0.93
MTX #1
DMSO #1
r = 0.60
MTX #2
DMSO #2
r = 0.63
d
DMSO
ACOT13
(ENST00000230048.5)
React.
>1.0
0.7
0.4
0.0
G/U
MTX
Conformation A
(77.65 ± 3.65%)
Conformation B
(22.35 ± 3.65%)
Conformation A
(100%)
e
log2(TEMTX / TEDMSO)
n.s.
8.6 x 10-3
< heterogeneity in MTX
> heterogeneity in MTX
= heterogeneity in MTX